Molybdenum isotopic evidence for the late accretion of outer Solar System material to Earth

Gerrit Budde*, Christoph Burkhardt, Thorsten Kleine

Institut für Planetologie, University of Münster, Wilhelm-Klemm-Straße 10, 48149 Münster, Germany.

*Correspondence to: gerrit.budde@uni-muenster.de

accepted for publication in

Nature Astronomy

https://doi.org/10.1038/s41550-019-0779-y

Earth grew through collisions with Moon- to Mars-sized planetary embryos from the inner Solar System, but it also accreted material from greater heliocentric distance[1,2], including carbonaceous chondrite-like bodies, the likely source of Earth's water and highly volatile species[3,4]. Understanding when and how this material was added to Earth is critical for constraining the dynamics of terrestrial planet formation and the fundamental process by which Earth became habitable. However, earlier studies inferred very different timescales for the delivery of carbonaceous chondrite-like bodies, depending on assumptions about the nature of Earth's building material[5-11]. Here we show that the molybdenum (Mo) isotopic composition of Earth's primitive mantle falls between those of the non-carbonaceous and carbonaceous reservoirs[12-15], and that this observation allows quantifying the accretion of carbonaceous chondrite-like material to Earth independent of assumptions about its building blocks. As most of the Mo in the primitive mantle was delivered by late-stage impactors[10], our data demonstrate that Earth accreted carbonaceous bodies late in its growth history, likely through the Moon-forming impact. This late delivery of carbonaceous material probably resulted from an orbital instability of the gas giant planets, and it demonstrates that Earth's habitability is strongly tied to the very late stages of its growth.

Nucleosynthetic isotope anomalies arise from the heterogeneous distribution of isotopically anomalous stellar-derived matter in the accretion disk and, as such, are a powerful tool to determine the nature and origin of Earth's building material[8,10,16-18]. However, current models utilizing these isotope anomalies to reconstruct Earth's accretion history and the delivery time of carbonaceous chondrite-like material are uncertain[18], because they rely on the contested[8,16,17] assumption that known meteorites represent Earth's building material[8-11]. Here we overcome this inherent uncertainty and present a new approach to this problem, which requires no assumptions about the isotopic composition of Earth's building material. Our approach uses the nucleosynthetic Mo isotope dichotomy between non-carbonaceous (NC) and carbonaceous (CC) meteorites, which represent two genetically distinct reservoirs that co-existed in the protoplanetary disk for several million years[12-15]. While the NC reservoir represents inner Solar System material, the CC reservoir was located at greater heliocentric distance, presumably beyond Jupiter's orbit[12,13,18], and includes carbonaceous chondrites, the likely source of Earth's water and highly volatile species[3,4]. Compared to NC meteorites, CC meteorites have an excess in nuclides produced in the rapid neutron capture process[12,13] (*r*-process) and possibly also the proton capture process[11,14] (*p*-process) of stellar nucleosynthesis. Additionally, meteorites from both groups exhibit variable abundances of Mo produced in the slow neutron capture process (*s*-process). Consequently, in a plot of ε^{94}Mo versus ε^{95}Mo (where ε^{i}Mo is the parts-per-10,000 deviation from a terrestrial Mo standard), NC and CC meteorites plot on two distinct *s*-process mixing lines (the NC- and CC-lines), where their offset reflects the *r*-process (and possibly *p*-process) excess of the CC reservoir (Fig. 1).

As Mo is a siderophile (iron-loving) element, most of the Mo in Earth's primitive mantle [hereafter referred to as "BSE" (bulk silicate Earth)] derives from the late stages of accretion, because Mo from earlier stages was largely removed into Earth's core[10]. Thus, if Earth received CC material only during early accretion stages, as proposed in previous studies[10,11], the BSE would plot on the NC-line. Conversely, if Earth accreted CC material during the latest

accretion stages, the BSE would plot off the NC- towards the CC-line. However, current data[11-15] do not define the slope and intercept of the NC-line or the BSE's Mo isotopic composition precisely enough to determine where the BSE plots.

We obtained Mo isotope data for many previously uninvestigated bulk meteorites, various terrestrial rock samples, and acid leachates from two primitive ordinary chondrites (Supplementary Table 1). The newly analysed bulk meteorites and the acid leachates plot on a single *s*-process mixing line together with enstatite and ordinary chondrites and several iron meteorites. The linear regression of the combined data is consistent with the NC-line observed in previous studies[11-15] but is now more precisely defined (Fig. 1; Supplementary Table 1). Importantly, the newly defined NC-line slope of 0.596±0.008 is identical to the slope of the CC-line (0.596±0.006), and both are consistent with the slope determined from Mo isotope measurements of presolar mainstream SiC grains (0.59)[19]. The fact that the NC- and CC-lines are parallel indicates that the Mo isotopic variability along them comes from heterogeneous distribution of the same or similar *s*-process carrier(s), and that the CC reservoir contains a constant *r*-process excess over the NC reservoir. Thus, the processes leading to the *s*-process variations evidently did not affect the *r*-process material in the two reservoirs, suggesting that this *r*-process material is not contained in individual presolar carriers; instead, the constant *r*-process difference between the CC and NC reservoirs reflects a characteristic isotopic difference between two bulk disk reservoirs[20].

It has been proposed that during the Solar System's first few million years, the composition of the inner disk (*i.e.*, the NC reservoir) changed continuously by admixture of outer Solar System material (*i.e.*, CC-derived material)[9]. If so, then later-formed NC bodies (*e.g.*, ordinary chondrites) should exhibit an *r*-process excess compared to earlier-formed NC bodies (*e.g.*, group IC, IIAB, IIIAB, IVA iron meteorites)[13]. However, all NC meteorites plot on the NC-line, indicating that they accreted from material with identical *r*-process proportions (Fig. 1). The NC-CC dichotomy, therefore, cannot reflect a secular change of inner disk composition[9], but instead results from efficient spatial separation of two genetically distinct source regions[12,13].

The terrestrial rock samples show indistinguishable Mo isotopic compositions, averaging at ε^{94}Mo = 0.04±0.06 and ε^{95}Mo = 0.10±0.04 (95% CI) relative to the in-house Mo solution standard (ε^{i}Mo ≡ 0) (Supplementary Information; Supplementary Table 1). The small offset from zero most likely results from non-exponential isotopic fractionation induced during production of the high-purity standard, as has been observed for other elements[21,22]. As such, the terrestrial rock samples, and not the solution standards, are used to estimate the BSE's Mo isotopic composition (Supplementary Information).

The BSE's position among the NC- and CC-lines (Figs. 1, 2) provides two first-order constraints on the nature of Earth's accreting material and how the provenance of this material evolved over time. First, because the BSE plots between the NC- and CC-lines, Earth must have accreted CC material during late stages of its growth; otherwise, the BSE would plot on the NC-line. Second, no combination of known meteorites yields the BSE's Mo isotopic composition, indicating that Earth incorporated material that is distinct from known meteorites and enriched in *s*-process Mo. One possibility is that this *s*-process-enriched material derives from the NC reservoir, and the BSE's Mo isotopic composition reflects a mixture between this material and known CC material (Fig. 2b). However, the isotopic similarity of Earth and enstatite chondrites (EC) for many elements suggests that the average isotopic composition of

Earth's accreting material was mostly similar to ECs[10]. As such, it is more likely that the *s*-process-enriched material derives from the CC reservoir, and the BSE's Mo isotopic composition reflects a mixture between this material and ECs (Fig. 2a). In this case, Earth's building material largely comprised objects with EC-like isotopic compositions[10], and isotopically distinct material was only added during late stages of accretion. The BSE's isotopic composition would then naturally be EC-like but would deviate preferentially for elements that were added late, such as Mo. For elements recording Earth's full accretion history (*e.g.*, Cr, Ti), the resulting changes would be small; assuming an EC-like isotopic composition for the proto-Earth, the addition of CC material during the last ~10% of accretion would have changed its ε^{54}Cr and ε^{50}Ti by only ~0.1–0.2, consistent with the small, albeit not resolved, difference between ECs and Earth for these two elements[18].

Regardless of such assumptions about the composition of Earth's building material, the relative contributions of NC and CC bodies to the BSE's Mo can be determined using the intercept theorem. As the NC- and CC-lines are parallel, the BSE composition divides any tie line between them into two segments whose ratio to each other is constant. Consequently, irrespective of the position of the endmembers on the NC- and CC-lines, the resulting mixing ratio between NC and CC material remains the same. Thus, unlike previous attempts[8-11,18], our approach for constraining the accretion of CC material to Earth is independent of the absolute isotope anomalies among Earth's accreting material.

To quantify the amount of CC material contributing to the BSE's Mo, we introduce the Δ^{95}Mo notation:

$$\Delta^{95}\mathrm{Mo} = (\varepsilon^{95}\mathrm{Mo} - 0.596 \times \varepsilon^{94}\mathrm{Mo}) \times 100 \qquad (1)$$

where the slope of 0.596 represents the slope of the NC- and CC-lines; Δ^{95}Mo provides the parts-per-million deviation of any *s*-process mixing line from the origin and is a measure for the *r*-process excess relative to the composition of the Mo standard. For the NC and CC reservoirs we find $\Delta^{95}\mathrm{Mo}_{\mathrm{NC}} = -9\pm2$ and $\Delta^{95}\mathrm{Mo}_{\mathrm{CC}} = +26\pm2$ (Supplementary Information; Supplementary Fig. 1), which are unique isotope signatures for these two reservoirs, irrespective of the absolute isotope anomaly of a given sample. The mass fraction of CC-derived Mo (f_{CC}) in the present-day BSE is then given by mass balance:

$$f_{\mathrm{CC}} = \frac{\Delta^{95}\mathrm{Mo}_{\mathrm{BSE}} - \Delta^{95}\mathrm{Mo}_{\mathrm{NC}}}{\Delta^{95}\mathrm{Mo}_{\mathrm{CC}} - \Delta^{95}\mathrm{Mo}_{\mathrm{NC}}} \qquad (2)$$

From the terrestrial rock samples, we determined $\Delta^{95}\mathrm{Mo}_{\mathrm{BSE}} = +7\pm5$ (Supplementary Information), corresponding to a mass fraction of CC-derived Mo in the BSE of 0.46±0.15. Thus, ~30–60% of the BSE's Mo derives from the CC reservoir. Note that the total fraction of CC material in the bulk Earth is likely much smaller, because Mo records only the late stages of Earth's accretion.

As most of the BSE's Mo derives from the last 10–20% of accretion[10], its isotopic composition should be strongly influenced by the Moon-forming impactor, the last large body thought to collide with Earth[23], and by the late veneer, the material added to Earth's mantle after the giant impact and cessation of core formation[24]. To quantify the contribution of these

components, we calculated the expected Δ^{95}Mo of the BSE for different assumed compositions of the Moon-forming impactor, the proto-Earth's mantle (Earth's mantle just before the giant impact), and the late veneer using a Monte Carlo approach (Supplementary Information). Several scenarios are considered in which pure CC, pure NC, or mixed NC-CC (*i.e.*, a BSE-like Δ^{95}Mo of 7±5) compositions are assumed for the three components (Fig. 3).

The BSE's Δ^{95}Mo is reproduced well when the Moon-forming impactor contains a significant amount of CC material (Fig. 4a). For instance, assuming a pure CC composition for the impactor reproduces the BSE's Δ^{95}Mo in >90% of the cases, provided that more than ~20% of the impactor core equilibrated with proto-Earth's mantle. For a mixed NC-CC composition of the Moon-forming impactor, the BSE's Δ^{95}Mo is reproduced in <20% of the cases, unless a mixed NC-CC composition is also assumed for the late veneer (Fig. 4a). By contrast, assuming a pure NC composition for the Moon-forming impactor provides the best match only for an impactor core re-equilibration of less than ~10% (Fig. 4b), because then most of the impactor's Mo is directly removed into Earth's core without contributing to the BSE's Mo. Although the degree of impactor core re-equilibration is poorly known, it was likely larger than ~40%[5,25]. Thus, there is only a small chance that the Moon-forming impactor had a pure NC composition; this holds true for all cases except if a pure CC composition for the late veneer is assumed (Fig. 4b). However, although Se/Te ratios[6] and Te isotopic compositions[26] suggest that the late veneer contained some CC material, the BSE's Ru and Os isotopic compositions are distinct from CC meteorites[8,27,28], demonstrating that the late veneer did not solely consist of CC bodies. Yet, assuming a mixed NC-CC composition for the late veneer does not provide a good match to the BSE's Δ^{95}Mo, even if a mixed NC-CC composition is also assumed for the proto-Earth's mantle (Fig. 4b). Thus, neither the late veneer nor the proto-Earth's mantle can be the sole source of CC material in the BSE. The CC material, therefore, was wholly or partly delivered by the Moon-forming impactor, which either had a pure CC or a mixed NC-CC composition.

A CC heritage of the Moon-forming impactor contrasts with the isotopic composition of the Moon itself, for which no CC signature has yet been found[22,29]. This implies that the Moon either formed from proto-Earth material[30,31] or equilibrated with Earth after the giant impact[32]. A CC heritage of the Moon-forming impactor also implies that, against current thinking[9,10], this body did not form in the inner Solar System but originated further away, probably beyond Jupiter's orbit (*i.e.*, the presumed location of the CC reservoir[12,13]). Consistent with this, dynamical models of terrestrial planet formation predict that due to the orbital evolution of the gas giant planets—either during an early migration[33] or a later orbital instability[34]—embryos from beyond ~2.5 AU were preferentially incorporated into Earth late, often with the final large impactor[2].

Assuming that the Moon-forming impactor had a pure CC composition and was Mars-sized[23], it would have added ~0.1 Earth masses of CC material. This amount would be lower if the impactor were smaller[31] or if it had a mixed NC-CC composition, which may have resulted from prior collisions between smaller NC and CC embryos. Nevertheless, although the Moon-forming impactor probably was not as volatile rich as CI chondrites, it still likely added the equivalent of 0.02±0.01 Earth masses of CI material necessary to account for Earth's budget of water and highly volatile species[4].

References (main text)

1. Morbidelli, A., Lunine, J. I., O'Brien, D. P., Raymond, S. N. & Walsh, K. J. Building terrestrial planets. *Ann. Rev. Earth Planet. Sci.* 40, 251-275 (2012).
2. O'Brien, D. P., Izidoro, A., Jacobson, S. A., Raymond, S. N. & Rubie, D. C. The Delivery of Water During Terrestrial Planet Formation. *Space Sci. Rev.* 214, 47 (2018).
3. Alexander, C. M. O. D. *et al.* The provenances of asteroids, and their contributions to the volatile inventories of the terrestrial planets. *Science* 337, 721-723 (2012).
4. Marty, B. The origins and concentrations of water, carbon, nitrogen and noble gases on Earth. *Earth Planet. Sci. Lett.* 313-314, 56-66 (2012).
5. Rubie, D. C. *et al.* Accretion and differentiation of the terrestrial planets with implications for the compositions of early-formed Solar System bodies and accretion of water. *Icarus* 248, 89-108 (2015).
6. Wang, Z. & Becker, H. Ratios of S, Se and Te in the silicate Earth require a volatile-rich late veneer. *Nature* 499, 328-331 (2013).
7. Albarede, F. Volatile accretion history of the terrestrial planets and dynamic implications. *Nature* 461, 1227-1233 (2009).
8. Fischer-Gödde, M. & Kleine, T. Ruthenium isotopic evidence for an inner Solar System origin of the late veneer. *Nature* 541, 525-527 (2017).
9. Schiller, M., Bizzarro, M. & Fernandes, V. A. Isotopic evolution of the protoplanetary disk and the building blocks of Earth and the Moon. *Nature* 555, 507 (2018).
10. Dauphas, N. The isotopic nature of the Earth's accreting material through time. *Nature* 541, 521-524 (2017).
11. Bermingham, K. R., Worsham, E. A. & Walker, R. J. New insights into Mo and Ru isotope variation in the nebula and terrestrial planet accretionary genetics. *Earth Planet. Sci. Lett.* 487, 221-229 (2018).
12. Budde, G. *et al.* Molybdenum isotopic evidence for the origin of chondrules and a distinct genetic heritage of carbonaceous and non-carbonaceous meteorites. *Earth Planet. Sci. Lett.* 454, 293-303 (2016).
13. Kruijer, T. S., Burkhardt, C., Budde, G. & Kleine, T. Age of Jupiter inferred from the distinct genetics and formation times of meteorites. *Proc. Nat. Acad. Sci.* 114, 6712-6716 (2017).
14. Poole, G. M., Rehkämper, M., Coles, B. J., Goldberg, T. & Smith, C. L. Nucleosynthetic molybdenum isotope anomalies in iron meteorites – new evidence for thermal processing of solar nebula material. *Earth Planet. Sci. Lett.* 473, 215-226 (2017).
15. Worsham, E. A., Bermingham, K. R. & Walker, R. J. Characterizing cosmochemical materials with genetic affinities to the Earth: Genetic and chronological diversity within the IAB iron meteorite complex. *Earth Planet. Sci. Lett.* 467, 157-166 (2017).
16. Burkhardt, C. *et al.* A nucleosynthetic origin for the Earth's anomalous ^{142}Nd composition. *Nature* 537, 394-398 (2016).
17. Render, J., Fischer-Gödde, M., Burkhardt, C. & Kleine, T. The cosmic molybdenum-neodymium isotope correlation and the building material of the Earth. *Geochem. Persp. Let.* 3, 170-178 (2017).
18. Warren, P. H. Stable-isotopic anomalies and the accretionary assemblage of the Earth and Mars: A subordinate role for carbonaceous chondrites. *Earth Planet. Sci. Lett.* 311, 93-100 (2011).

19. Nicolussi, G. K. *et al.* Molybdenum isotopic composition of individual presolar silicon carbide grains from the Murchison meteorite. *Geochim. Cosmochim. Acta* 62, 1093-1104 (1998).
20. Nanne, J. A. M., Nimmo, F., Cuzzi, J. N. & Kleine, T. Origin of the non-carbonaceous–carbonaceous meteorite dichotomy. *Earth Planet. Sci. Lett.* 511, 44-54 (2019).
21. Steele, R. C. J., Elliott, T., Coath, C. D. & Regelous, M. Confirmation of mass-independent Ni isotopic variability in iron meteorites. *Geochim. Cosmochim. Acta* 75, 7906-7925 (2011).
22. Zhang, J. J., Dauphas, N., Davis, A. M., Leya, I. & Fedkin, A. The proto-Earth as a significant source of lunar material. *Nature Geosci.* 5, 251-255 (2012).
23. Canup, R. M. & Asphaug, E. Origin of the Moon in a giant impact near the end of the Earth's formation. *Nature* 412, 708-712 (2001).
24. Walker, R. J. Highly siderophile elements in the Earth, Moon and Mars: Update and implications for planetary accretion and differentiation. *Chem Erde-Geochem.* 69, 101-125 (2009).
25. Rudge, J. F., Kleine, T. & Bourdon, B. Broad bounds on Earth's accretion and core formation constrained by geochemical models. *Nature Geosci.* 3, 439-443 (2010).
26. Fehr, M. A., Hammond, S. J. & Parkinson, I. J. Tellurium stable isotope fractionation in chondritic meteorites and some terrestrial samples. *Geochim. Cosmochim. Acta* 222, 17-33 (2018).
27. Bermingham, K. R. & Walker, R. J. The ruthenium isotopic composition of the oceanic mantle. *Earth Planet. Sci. Lett.* 474, 466-473 (2017).
28. Meisel, T., Walker, R. J. & Morgan, J. W. The osmium isotopic composition of the Earth's primitive upper mantle. *Nature* 383, 517-520 (1996).
29. Akram, W. & Schönbächler, M. Zirconium isotope constraints on the composition of Theia and current Moon-forming theories. *Earth Planet. Sci. Lett.* 449, 302-310 (2016).
30. Canup, R. M. Forming a Moon with an Earth-like Composition via a Giant Impact. *Science* 338, 1052-1055 (2012).
31. Cuk, M. & Stewart, S. T. Making the Moon from a Fast-Spinning Earth: A Giant Impact Followed by Resonant Despinning. *Science* 338, 1047-1052 (2012).
32. Lock, S. J. *et al.* The Origin of the Moon Within a Terrestrial Synestia. *J. Geophys. Res.* 123, 910-951 (2018).
33. O'Brien, D. P., Walsh, K. J., Morbidelli, A., Raymond, S. N. & Mandell, A. M. Water delivery and giant impacts in the 'Grand Tack' scenario. *Icarus* 239, 74-84 (2014).
34. O'Brien, D. P., Morbidelli, A. & Levison, H. F. Terrestrial planet formation with strong dynamical friction. *Icarus* 184, 39-58 (2006).

Acknowledgments: We are grateful to NASA and the Institute of Meteoritics, University of New Mexico, for providing samples. We are also grateful to K. Metzler, G. Brennecka, and A. Bischoff for discussions, C. Brennecka for comments on the paper, U. Heitmann for technical support, as well as R. Walker and K. Bermingham (University of Maryland) for providing their Mo solution standard. This study was supported by the European Research Council Consolidator Grant "ISOCORE" (contract 616564) and by the Deutsche Forschungsgemeinschaft (SFB/TRR 170 subproject B3-1). This is TRR publication no. 61.

Author Contributions: G.B., C.B., and T.K. devised the study. G.B. prepared the samples for Mo isotope analyses and performed all measurements. All authors contributed to the interpretation of the data and preparation of the manuscript.

Competing interests: The authors declare no competing interests.

Data availability: All data generated during this study are included in this published article (and its Supplementary Information files).

Correspondence and requests for materials should be addressed to G.B.

Figure captions

Fig. 1. Molybdenum isotope dichotomy of meteorites in ε^{95}Mo versus ε^{94}Mo space. Carbonaceous (CC, blue) and non-carbonaceous (NC, red) meteorites define two parallel lines with identical slopes. Samples from both groups show variable *s*-process deficits relative to the terrestrial standard (ε^{95}Mo ≡ 0, ε^{94}Mo ≡ 0), resulting in isotope variations along each line. The offset between the two lines results from a constant *r*-process excess in the CC reservoir. The bulk silicate Earth (BSE, green) plots between the NC- and CC-lines, demonstrating that the BSE's Mo derives from both the NC and CC reservoirs. Open symbols represent literature data (Supplementary Table 4), closed symbols are data from this study. Error envelopes and error bars typically represent 95% confidence intervals (95% CI).

Fig. 2. Two potential scenarios for reproducing the BSE's Mo isotopic composition. **a**, Mixing between enstatite chondrite-like material and presumed *s*-process-enriched CC material. **b**, Mixing between presumed *s*-process-enriched NC material and a CC component having a typical composition of carbonaceous meteorites (ε^{94}Mo ≈ 1.15; ε^{95}Mo ≈ 0.95). In both scenarios an unknown component with an *s*-process excess is required to balance the *s*-process deficit observed for known meteorites. For clarity, only selected meteorite groups are shown (EC: enstatite chondrites, OC: ordinary chondrites, IAB: IAB iron meteorite); shaded areas represent ranges of bulk meteorites, where the widths of these areas correspond to the uncertainties on the CC- and NC-lines (see Fig. 1). Error bars typically represent 95% confidence intervals (95% CI).

Fig. 3. Predicted Δ^{95}Mo of the BSE versus the degree of impactor core re-equilibration during the Moon-forming impact. Grey horizontal bar represents the BSE's Δ^{95}Mo = 7±5; dots represent outcomes of Monte Carlo simulations of the predicted Δ^{95}Mo resulting from mixing between proto-Earth's mantle (pE), the Moon-forming impactor (GI), and the late veneer (LV) of different compositions (Supplementary Information). **a–c**, A CC component in the Moon-forming impactor is assumed, while a pure NC composition is assumed for proto-Earth's mantle. **d–f**, A pure NC composition is assumed for the Moon-forming impactor, while a CC component is present in the late veneer and/or proto-Earth's mantle.

Fig. 4. Probability for matching the BSE's Δ^{95}Mo for different compositions of proto-Earth's mantle, the Moon-forming impactor, and the late veneer as a function of impactor core re-equilibration during formation of the Moon. Probabilities calculated using the results from the modelling shown in Fig. 3. **a**, Probabilities for the scenarios in which the Moon-forming impactor always contains CC material (Fig. 3a–c). **b**, Probabilities for the scenarios in which the Moon-forming impactor always has a pure NC composition (Fig. 3d–f).

Methods

Sample preparation and digestion of bulk meteorites and terrestrial samples. The meteorite samples investigated in the present study are summarized in Supplementary Table 1 and include different carbonaceous (CK, CH, CB) and Rumuruti chondrites as well as numerous groups of achondrites, such as acapulcoites, angrites, aubrites, brachinites, mesosiderites, and ureilites (including two ureilitic fragments from the Almahata Sitta meteorite named "MS-MU-17" and "MS-MU-20"), as well as the ungrouped achondrites Tafassasset and NWA 1058. For almost all of these groups of meteorites no high-precision Mo isotopic data have been reported before.

Pieces of these meteorites (~0.3–2 g) were carefully cleaned by polishing with SiC as well as sonication in ethanol, and then ground to a fine powder in an agate mortar. Since bulk aubrites have very low Mo concentrations (~10 ppb), a ~10.5 g piece of Peña Blanca Spring and ~0.5 g of a metal nodule from Norton County were used. Bulk meteorite samples as well as terrestrial rock standards were digested in Savillex® vials on a hotplate using HF–HNO_3–$HClO_4$ (2:1:0.01) at 180–200 °C (5 days), followed by inverse aqua regia (2:1 HNO_3–HCl) at 130–150 °C (2 days) and repeated dry-downs with 6 M HCl–0.06 M HF.

Leaching procedure for ordinary chondrites. Pieces of the unequilibrated ordinary chondrites (UOC) NWA 2458 (L3.2; 6.48g) and WSG 95300 (H3.3; 4.35g) were carefully cleaned by polishing with SiC as well as sonication in ethanol, and then ground to a fine powder in an agate mortar. Thereafter, these powders were subjected to a sequential (six-step) leaching procedure in Savillex® vials as summarized in Supplementary Table 3, which was modified from ref. 35. Only ultrapure water (Milli-Q®) and twice-distilled (HCl, HNO_3, HF) or 'suprapur' (HAc, $HClO_4$) acids were used, and a blank was processed through the entire leaching procedure together with the two samples. In addition to the acid leachates, a whole rock sample of NWA 2458 was also analysed (as described above).

After each leaching step, the samples were centrifuged at 4400 rpm (~2900 g) for 30 minutes and the supernatant was separated from the precipitate. The precipitate was rinsed 4–5 times with 5–10 ml H_2O to remove the remaining acid, where each rinse step was followed by centrifuging and separating the rinse from the precipitate. All rinse steps were combined with the corresponding supernatant to the final leachate, and the remaining precipitate was then subjected to the next leaching step. Note that after sub-step L6a (HF–HNO_3–$HClO_4$) the samples were dried down and $HClO_4$ was removed by repeated dry-downs with HNO_3 at 180–200 °C before adding inverse aqua regia (L6b). After sub-step L6b, the samples were centrifuged (see above), leaving behind a small amount of insoluble residue that was not further investigated.

At this stage, small aliquots (~2%) of all leachates were taken to determine Mo contents. The aliquots were dried down, treated with inverse aqua regia to attack organics, and dissolved in 0.5 M HNO_3–0.01 M HF. Mo contents were then measured on a Thermo Scientific® XSeries 2 quadrupole ICP-MS. Depending on the amount of Mo present, 30–90% splits of the leachates were used for the Mo isotope composition analyses. These were dried down and treated with inverse aqua regia to attack organics, followed by repeated dry-downs with 6 M HCl–0.06 M HF.

Chemical separation of Mo. The chemical separation of Mo was accomplished following the analytical protocol described in refs. 12, 36. First, Mo was separated from most of the sample matrix using a two-stage anion exchange chromatography. In the first stage, the samples were typically loaded in 75 ml 0.5 M HCl–0.5 M HF onto columns filled with 4 ml of pre-cleaned Bio-Rad® AG1-X8 anion exchange resin (200–400 mesh). Most of the sample matrix was washed off the columns with the loading solution and additional 10 ml 0.5 M HCl–0.5 M HF. The high field strength elements (HFSE) and W were then eluted in 15 ml 6 M HCl–1 M HF, while Mo largely (~85%) remained on the resin, and was subsequently collected using 10 ml 3 M HNO_3. To prevent overloading the columns, samples of more than ~0.5 g (*e.g.*, ureilites, NWA 4931, L1/L2/L6 leachates) were dissolved in 150–300 ml 0.5 M HCl–0.5 M HF and then processed consecutively in 2–4 splits (equivalent to ~0.5 g sample each) through the first anion exchange chromatography (the same column and resin were re-used for all splits of the same sample, and both the HFSE and the Mo cuts from the different splits were re-combined afterwards). The Peña Blanca Spring sample (~10.5 g) was loaded in a total of 1500 ml 0.5 M HCl–0.5 M HF and processed as described above, albeit using several columns (20 splits). Note that this procedure neither affected the total yield nor the accuracy of the isotope data, which is demonstrated by the Mo isotope composition of the Peña Blanca Spring sample being indistinguishable from that of the Norton County metal nodule.

A small fraction (~15%) of the Mo is typically eluted together with the HFSEs. This Mo was recovered during the second stage, where all samples were loaded in 6 ml 0.6 M HF–0.4% H_2O_2 onto Bio-Rad® Poly-Prep columns containing 1 ml of pre-cleaned AG1-X8 resin (200–400 mesh). The columns were then rinsed with 10 ml 1 M HCl–2% H_2O_2, 9 ml 8 M HCl–0.01 M HF, 0.5 ml 6 M HCl–1 M HF, and 8.5 ml 6 M HCl–1 M HF to quantitatively remove the HFSEs, followed by elution of Mo with 5 ml 3 M HNO_3.

The Mo cuts from both stages were then combined, and Mo concentrations as well as the purity of the samples were determined on small aliquots (equivalent to ~5 ng Mo) of the combined Mo cuts by quadrupole ICP-MS. At this stage, samples with high Fe/Mo (*e.g.*, ureilites, L1/L6 leachates), Ru/Mo (L2 leachates), or Nb/Mo (JA-2, JG-1, W-2a) were further purified with an additional anion exchange chromatography, which was slightly modified from ref. 37. For the clean-up, the respective samples were loaded in 7 ml 1 M HF onto Bio-Rad® Poly-Prep columns containing 2 ml of pre-cleaned AG1-X8 resin (100–200 mesh). The columns were then rinsed with 14 ml 1 M HF, 20 ml 6 M HCl–0.06 M HF, and 8 ml 6 M HCl–1 M HF to quantitatively remove Fe, Ru, and remaining HFSE (particularly Nb) from the Mo cuts.

The final purification of Mo was performed using a two-stage ion exchange chromatography that was slightly modified from ref. 37. The samples were loaded in 1 ml 1 M HCl onto columns filled with 1 ml pre-cleaned Eichrom® TRU Resin (100–150 µm) and, after rinsing with 6 ml 1 M HCl, Mo was eluted in 6 ml 0.1 M HCl. This chemistry was repeated once, but using 7 M HNO_3 and 0.1 M HNO_3 instead of 1 M HCl and 0.1 M HCl, respectively. The Mo cuts from all ion chromatography steps were evaporated with added HNO_3 and inverse aqua regia to destroy organic compounds. The Mo yield for the entire procedure was typically ~75%, and total procedural blanks were typically ~2–4 ng Mo and thus negligible. Only for the L6 leachates the blank of ~11 ng was significant and required a small blank correction of ~1ε on ε^{92}Mo. We note, however, that this blank correction has no effect on the interpretation of the Mo isotope data, particularly the ε^{95}Mo–ε^{94}Mo systematics.

Mo isotope measurements. The Mo isotope compositions were measured on a Thermo Scientific® Neptune *Plus* multicollector inductively coupled plasma mass spectrometer in the Institut für Planetologie at the University of Münster, and followed the measurement protocol described in refs. 12, 36. Sample solutions were introduced into the mass spectrometer using a self-aspirating Savillex® C-Flow PFA nebulizer (~50 µl/min uptake rate) connected to a Cetac® Aridus II desolvator. The measurements were performed in low-resolution mode using standard Ni sampler and (H) skimmer cones, which yielded total ion beam intensities of ~1.1×10^{-10} A for a ~100 ppb Mo solution. Each measurement consisted of 40 baseline integrations (on-peak zeros) of 8.4 s each followed by 100 Mo isotope ratio measurements of 8.4 s each, which consumed ~80 ng of Mo. All data were corrected for instrumental mass bias by internal normalization to $^{98}Mo/^{96}Mo = 1.453173$ using the exponential law, because this normalization results in large Mo isotope anomalies and distinctive isotope patterns[37]. Small isobaric interferences of Zr and Ru on Mo masses were corrected by monitoring interference-free ^{91}Zr and ^{99}Ru. The final Mo cuts typically had Ru/Mo and Zr/Mo of $<1\times10^{-4}$, where the interference corrections for Ru (on $\varepsilon^{100}Mo$) and Zr (on $\varepsilon^{94}Mo$) were always <2ε, respectively. Note that Zr interference corrections of up to ~25ε (Zr/Mo ≈ 1.4×10^{-3}) and Ru interference corrections of >20ε (Ru/Mo ≈ 2.1×10^{-3}) are accurate to within analytical uncertainty[12].

The Mo isotope ratios are reported as $\varepsilon^{i}Mo$ values, which represent the parts-per-10,000 deviation of a sample from the mean of the bracketing runs of the Alfa Aesar® solution standard, where $\varepsilon^{i}Mo = [(^{i}Mo/^{96}Mo)_{sample} / (^{i}Mo/^{96}Mo)_{standard} - 1] \times 10^{4}$ (i = 92, 94, 95, 97, 100). For samples analysed multiple times, the reported $\varepsilon^{i}Mo$ values represent the mean of pooled solution replicates together with their associated external uncertainties. The external reproducibility of the Mo isotope measurements ranges from ±0.15 for $\varepsilon^{97}Mo$ to ±0.35 for $\varepsilon^{92}Mo$ (2 s.d.), as defined by repeated analyses of the BHVO-2 rock standard, several digestions of which were processed through the full analytical procedure and analysed together with each set of samples (Supplementary Table 2).

Since some previous studies reported Mo isotope data relative to different solution standards, we measured the composition of the NIST SRM 3134 (*e.g.*, ref. 14) and Alfa Aesar Specpure® Plasma (*e.g.*, refs. 11, 15) standards relative to the Alfa Aesar solution standard used in Münster. Repeated analyses of these standards during multiple measurement sessions demonstrate that all these solution standards have indistinguishable Mo isotopic compositions (Supplementary Table 1). Furthermore, in order to demonstrate the accuracy of our procedure, we processed our Alfa Aesar and the NIST SRM 3134 solution standards as well as different digestions of the DTS-2b rock standard that were doped with our Alfa Aesar standard (DTS-2b is extremely depleted in Mo and thus >90% of the measured mixture is from the Alfa Aesar standard) through the full analytical protocol described above. All processed solution standards are indistinguishable from the unprocessed solution standards (Supplementary Table 1), demonstrating that the chemical separation does not induce any resolvable effects on the measured Mo isotope compositions.

References (Methods)

35. Reisberg, L. *et al*. Nucleosynthetic osmium isotope anomalies in acid leachates of the Murchison meteorite. *Earth Planet. Sci. Lett.* **277**, 334-344 (2009).
36. Budde, G., Kruijer, T. S. & Kleine, T. Hf-W chronology of CR chondrites: Implications for the timescales of chondrule formation and the distribution of ^{26}Al in the solar nebula. *Geochim. Cosmochim. Acta* **222**, 284-304 (2018).
37. Burkhardt, C. *et al*. Molybdenum isotope anomalies in meteorites: Constraints on solar nebula evolution and origin of the Earth. *Earth Planet. Sci. Lett.* **312**, 390-400 (2011).

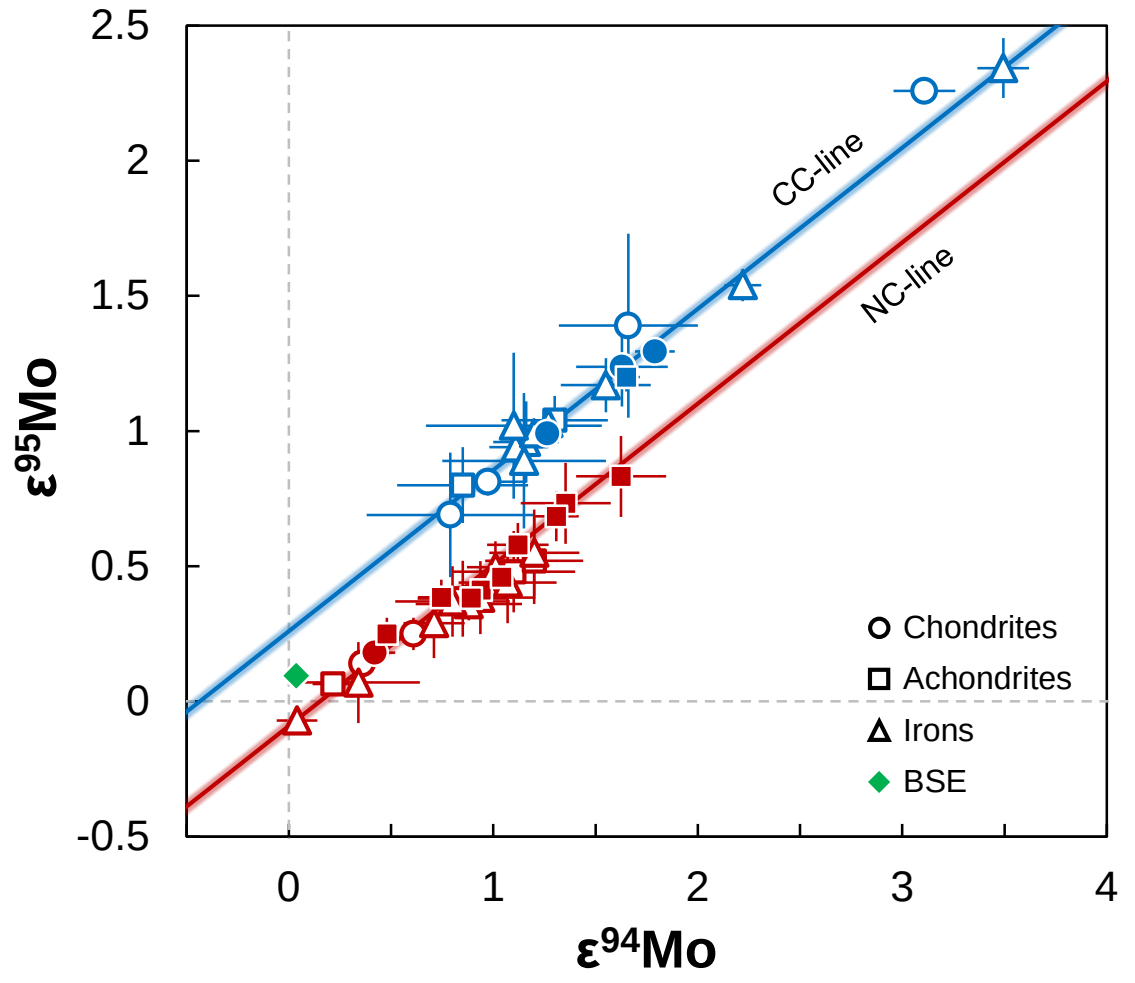
2.5
2
1.5
1
0.5
0
-0.5
0
1
2
3
4
ε95Mo
ε94Mo
CC-line
NC-line
Chondrites
Achondrites
Irons
BSE

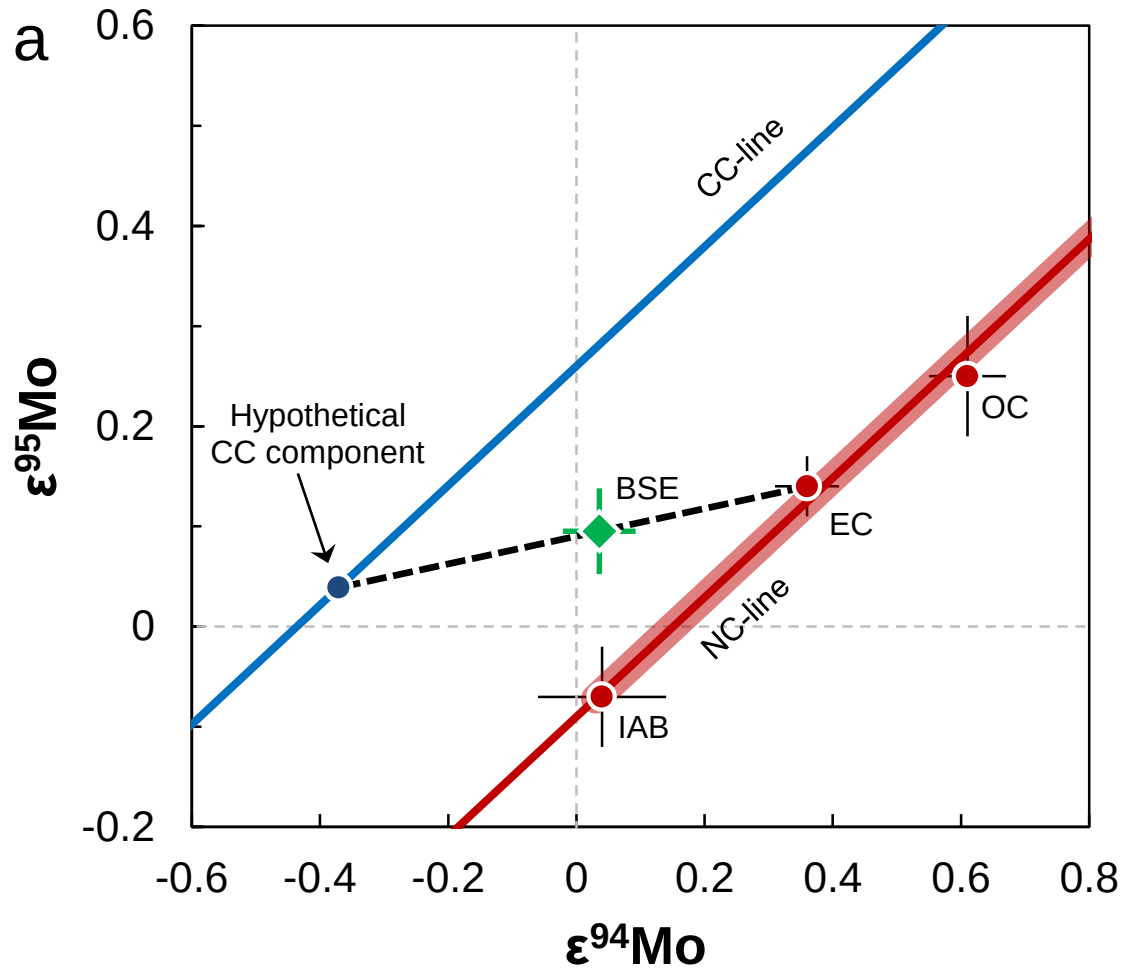
a
CC-line
Hypothetical
CC component
BSE
OC
EC
NC-line
IAB
ε95Mo
ε94Mo
0.6
0.4
0.2
0
-0.2
-0.6
-0.4
-0.2
0
0.2
0.4
0.6
0.8

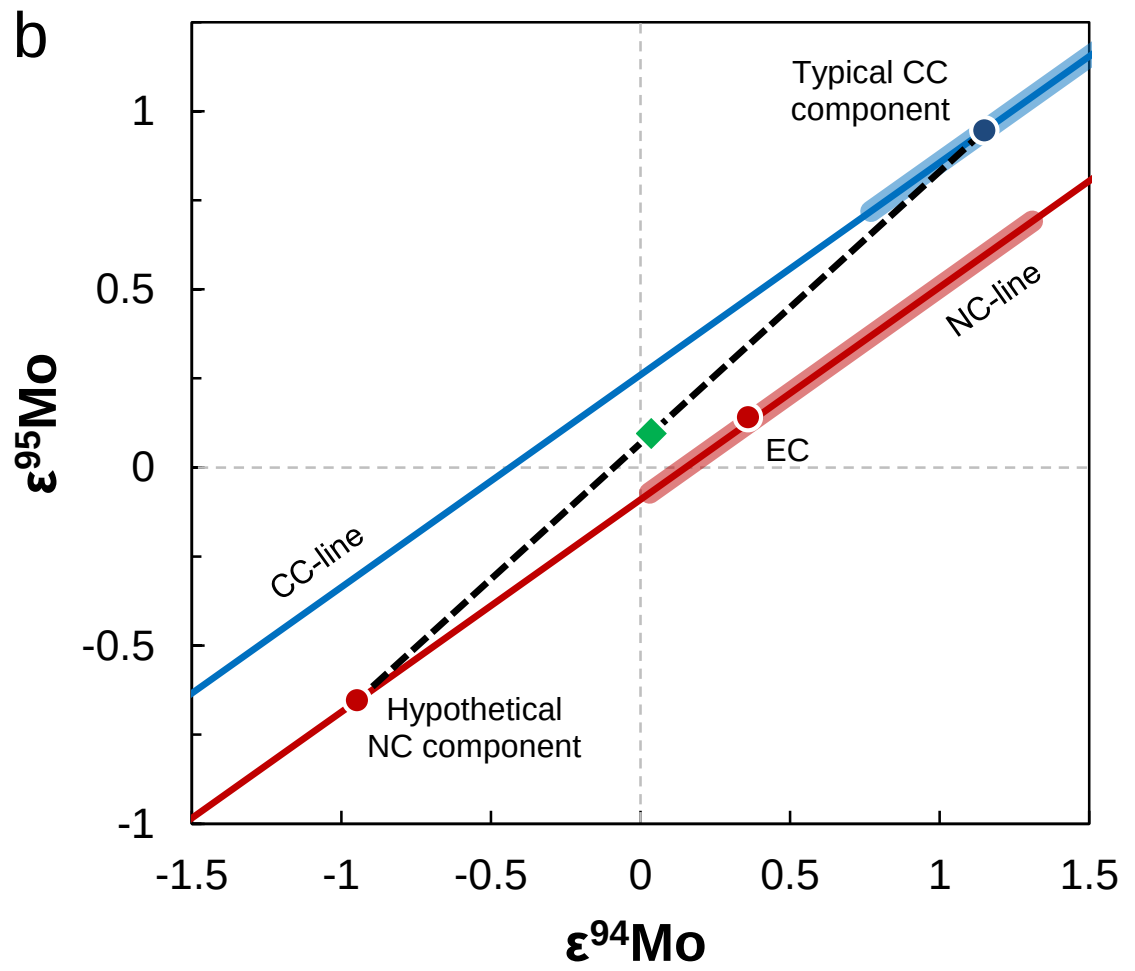
b
Typical CC
component
NC-line
EC
CC-line
Hypothetical
NC component
ε95Mo
ε94Mo
1
0.5
0
-0.5
-1
-1.5
-1
-0.5
0
0.5
1
1.5

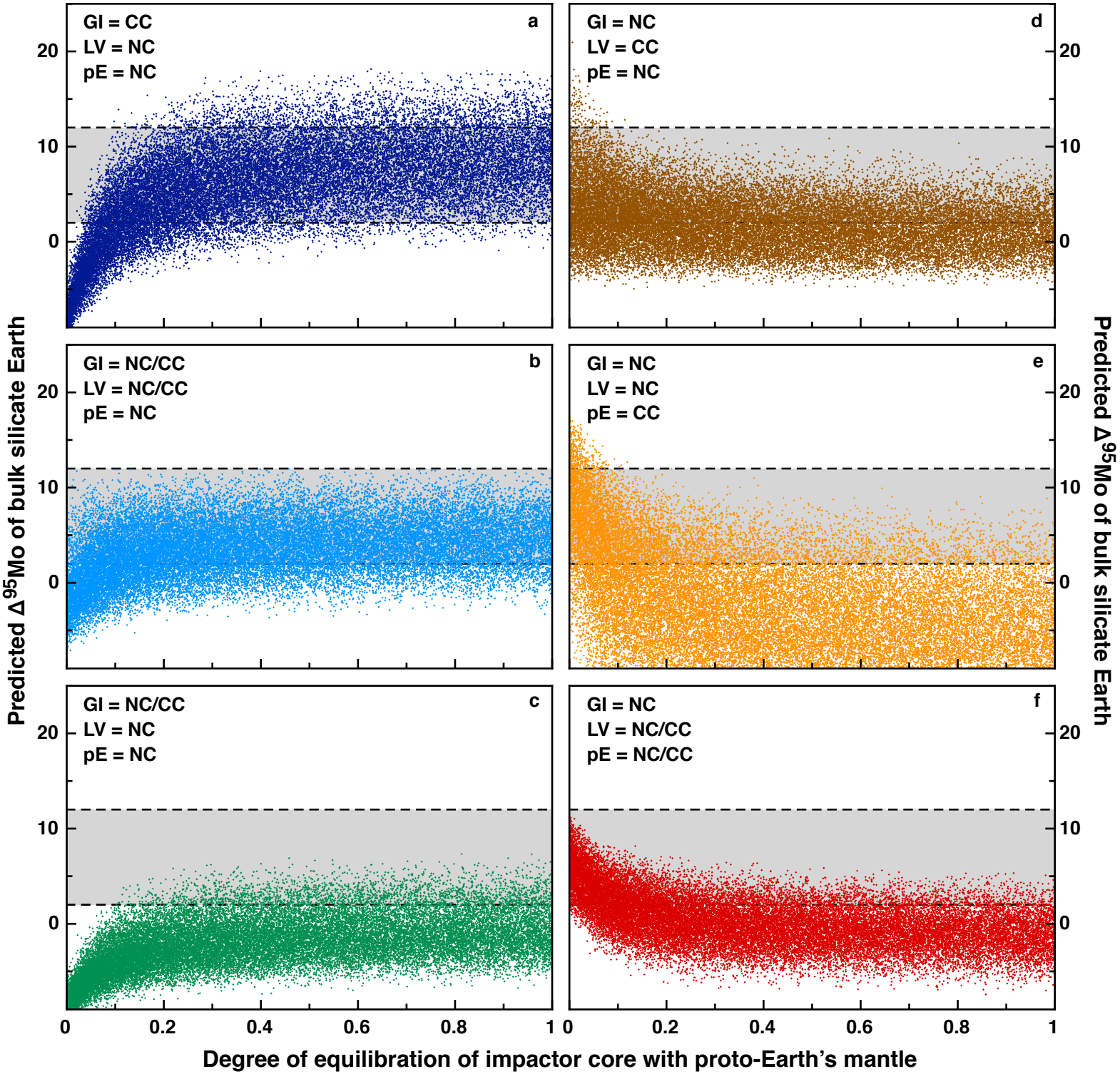
GI = CC
LV = NC
pE = NC
a
GI = NC/CC
LV = NC/CC
pE = NC
b
GI = NC/CC
LV = NC
pE = NC
c
GI = NC
LV = CC
pE = NC
d
GI = NC
LV = NC
pE = CC
e
GI = NC
LV = NC/CC
pE = NC/CC
f
Predicted Δ95Mo of bulk silicate Earth
Degree of equilibration of impactor core with proto-Earth's mantle
0
0.2
0.4
0.6
0.8
1
10
20

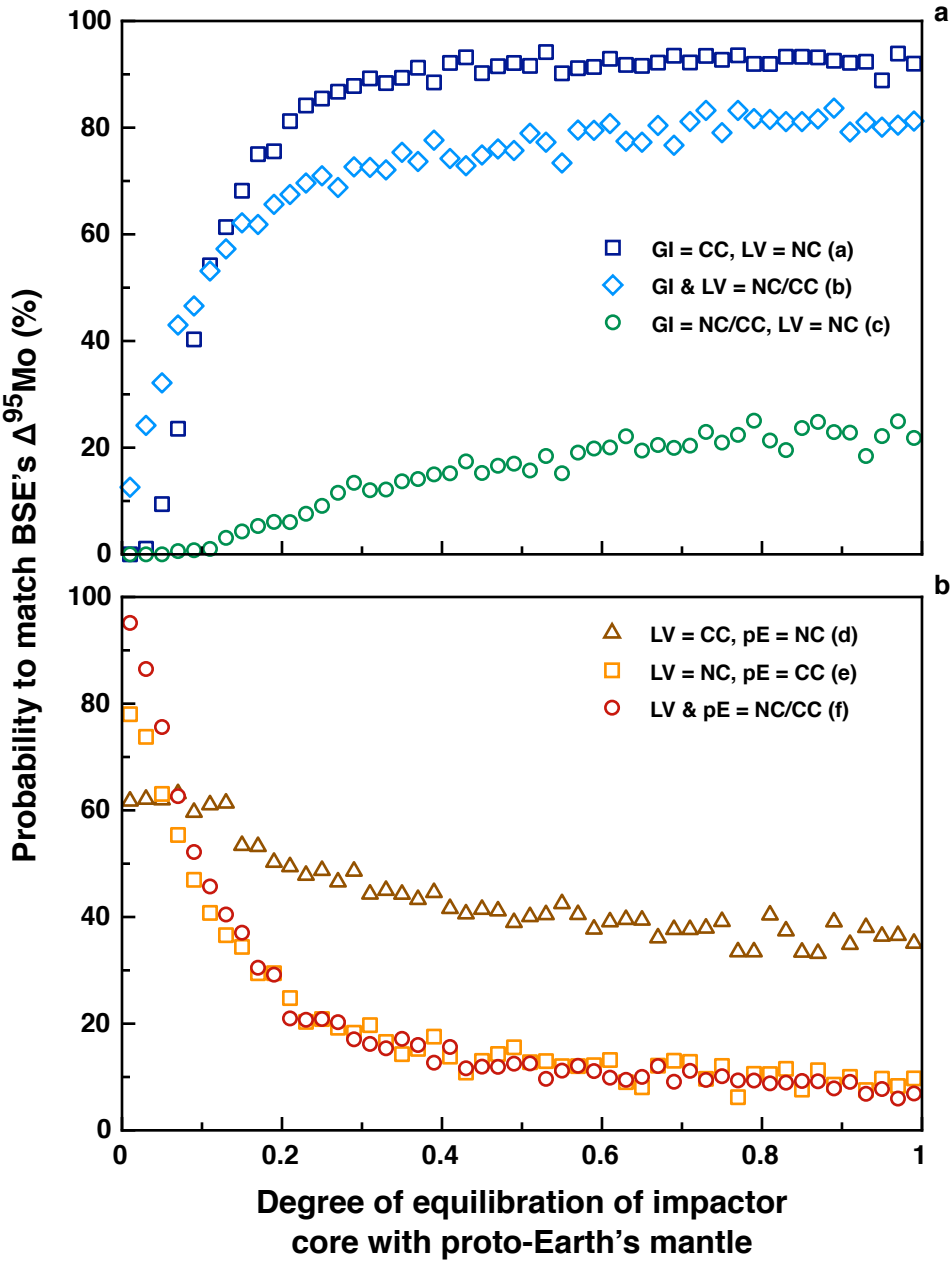
a
b
GI = CC, LV = NC (a)
GI & LV = NC/CC (b)
GI = NC/CC, LV = NC (c)
LV = CC, pE = NC (d)
LV = NC, pE = CC (e)
LV & pE = NC/CC (f)
Probability to match BSE's Δ95Mo (%)
Degree of equilibration of impactor core with proto-Earth's mantle
0
20
40
60
80
100
0.2
0.4
0.6
0.8
1

Supplementary Information

Molybdenum isotopic evidence for the late accretion of outer Solar System material to Earth

G. Budde, C. Burkhardt, T. Kleine

This file includes:
Supplementary Methods and Discussion
Supplementary Figures 1–6
Supplementary Tables 1–4

S1 Mo isotope data

The Mo concentration and isotope data obtained for terrestrial samples, bulk meteorites, and acid leachates are provided in Supplementary Table 1. Molybdenum concentrations of the analysed bulk meteorites typically range between ~0.2 and ~2 ppm. The amounts of Mo released in the various leachate steps of the unequilibrated ordinary chondrites (UOC) are highly variable (Supplementary Fig. 3). While the least Mo is released in the L1 and L6 steps, the largest fraction of Mo is released in the L2 (NWA 2458) or L5 (WSG 95300) steps. For NWA 2458 the total amount of Mo released (~3960 ng) in the leaching steps is consistent with the amount expected from the whole rock analyses (*i.e.*, >90% of the expected Mo was released during the leaching procedure).

All meteorite samples investigated here display well-resolved Mo isotope anomalies relative to the bracketing standard (ε^{i}Mo ≡ 0), the magnitude of which decrease in the order ε^{92}Mo > ε^{94}Mo > ε^{95}Mo > ε^{100}Mo > ε^{97}Mo. Independent of the magnitude of the anomalies, all samples exhibit the typical *w*- or *m*-shaped Mo isotope patterns that are indicative of a deficit or excess, respectively, in *s*-process Mo nuclides (*e.g.*, ref. 37) (Supplementary Fig. 4). In diagrams of ε^{i}Mo versus ε^{i}Mo (*e.g.*, Supplementary Fig. 5; Fig. 1) all samples generally plot along mixing lines between terrestrial Mo and a presumed component depleted (or enriched) in *s*-process Mo as measured in mainstream SiC grains[19]. Therefore, the measured Mo isotope anomalies are nucleosynthetic in origin, predominantly reflecting the heterogeneous distribution of an *s*-process carrier.

The anomalies in the bulk meteorites range between ε^{92}Mo ≈ 0.5 (RC, aubrites) and ε^{92}Mo ≈ 2.3 (CK, CH, Tafassasset), and samples from a given meteorite group typically have indistinguishable Mo isotope anomalies; the only exception are ureilites, which show some

resolved variability. While most ureilite samples cluster around an ε^{92}Mo of ~1 and mostly overlap within uncertainty, two monomict ureilites (EET 87517, PCA 82506) are characterized by significantly larger ε^{i}Mo excesses. These two samples were thus not included in the ureilite average (Supplementary Table 1) and plotted as individual points in Fig. 1. The nucleosynthetic isotope variability among ureilites likely results from the separation of isotopically distinct phases during partial differentiation of the ureilite parent body, as previously observed for Os isotopes[38]. As such, it remains unclear as to whether the calculated average is representative for the original bulk Mo isotopic composition of the ureilite parent body. However, all individual ureilites plot on the NC-line as defined below (Section S2), and so the observed variability among them is caused by variable deficits in *s*-process Mo nuclides. Thus, even if the bulk Mo isotopic composition of the original ureilite parent body was different from that measured for ureilites themselves, it would still plot on the NC-line.

Compared to bulk meteorites, the ordinary chondrite leachates display a much larger range of anomalies with ε^{92}Mo values between about –25 and +8. Consistent with the disparate Mo release patterns, the UOC samples also show very different Mo isotope compositions for the respective leachate steps (Supplementary Fig. 3). NWA 2458 is characterized by an overall trend from positive ε^{i}Mo values in the initial leachates to negative ε^{i}Mo values in the last leachate steps. In contrast, for WSG 95300 the Mo isotope anomalies appear arbitrarily distributed among the different leaching steps. For instance, the L3 step shows the largest *s*-process excess, whereas the L6 step displays the largest *s*-process deficit. The origin of the disparate isotope systematics in the L and H chondrite leachates is unclear at this point, but is probably is related to the redistribution of presolar components during nebular or parent-body processes. Nevertheless, the leachates plot on single well-defined correlation lines in ε^{i}Mo–ε^{i}Mo diagrams and, therefore, allow for the precise determination of the slopes of these lines (Supplementary Fig. 5). Only the leachate step L6 from WSG 95300 stands out by deviating from these correlation lines and is thus excluded from further discussion. Note, however, that including this leachate would yield identical results, albeit with larger uncertainties, for the NC-line regression (Section S2).

In a diagram of ε^{95}Mo versus ε^{94}Mo, in which the difference between *s*- and *r*-process variations is most pronounced, the analysed carbonaceous chondrites (CK, CH, CB) and Tafassasset plot on a distinct *s*-process mixing line than the other meteorites (Fig. 1). This observation is consistent with previous studies[11-15], which demonstrated that carbonaceous (CC) meteorites are characterized by a positive offset relative to non-carbonaceous (NC) meteorites in the ε^{95}Mo–ε^{94}Mo diagram, which most likely reflects an approximately constant *r*-process excess[12] or, alternatively, coupled *r*- and *p*-process excesses[14] in CC over NC materials. In contrast, all other bulk meteorites and the acid leachates analysed in the present study plot on a correlation line with enstatite and ordinary chondrites as well as most iron meteorites and other achondrites (see Section S2 for definition of NC-line), demonstrating that all these samples (*i.e.*, Rumuruti chondrites, acapulcoites, angrites, aubrites, brachinites, mesosiderites, ureilites, and the ungrouped achondrite NWA 1058) belong to the NC group of meteorites. Therefore, the new data presented here confirm and extend the fundamental dichotomy between CC and NC materials observed in previous studies to a much larger range of meteorite groups. So far, the Mo isotope dichotomy holds for all analysed samples (more than 40 meteorite groups and ungrouped meteorites; Supplementary Table 4), where the fact that all meteorites plot on either the CC- or the NC-line (and not in between) supports an efficient separation of two genetically distinct source regions of planetesimals.

S2 Calculation of CC- and NC-lines

The Mo isotopic data from this study, combined with previously reported results, allow a more precise calculation of the slopes and intercepts of the NC- and CC-lines. All regressions were calculated using the 'Model 1 fit' of *Isoplot* (v3.76), which is a York regression weighting the data points proportional to the inverse square of their assigned errors, where the reported uncertainties represent 95% confidence intervals (95% CI). The CC-line (Carbonaceous Chondrite-line) has already been precisely defined in prior studies using different kinds of sub-samples from carbonaceous chondrites (such as acid leachates and component-specific separates), all of which plot on the CC-line and, thus, have the same *r*-excess that is characteristics for CC materials in general[12,36]. For consistency, however, the CC-line was also recalculated using the same regression method, and including the new data for carbonaceous meteorites from this study.

A summary of all the bulk meteorite data used for the regressions, including data from this and previous studies, is provided in Supplementary Table 4. Note that the Mo isotopic composition of iron meteorites may have been modified owing to interaction with galactic cosmic rays (GCR)[11,15]. For the definition of the NC- and CC-lines we, therefore, only used data for iron meteorites for which such effects were corrected or are negligible, as demonstrated by minor to absent GCR effects on Pt and Os isotopes.

Some prior studies have argued that the nucleosynthetic isotope composition of primitive chondrites may not reflect that of the original bulk body, because alteration on the parent body may have mobilized and redistributed isotopically anomalous Mo from presolar phases[11,39]. In addition, owing to the presence of isotopically anomalous components, primitive chondrites may be isotopically heterogeneous at the sampling scale. These issues likely do not exist with iron meteorites because they formed by large-scale melting and metal segregation, which led to complete homogenization of presolar phases prior to metal-silicate fractionation. As noted above, however, among the differentiated meteorites, the isotopic composition of ureilites may not be representative for that of the bulk parent body. Nevertheless, all analysed bulk meteorites plot along either the NC- or the CC-line, indicating that the isotopic variations within each group predominantly reflect *s*-process variations. Thus, any unrepresentative sampling of bulk parent body compositions, if it occurred, only resulted in variations along either NC- or the CC-line, but not in significant deviations from either of the lines. Consequently, for the purpose of defining the slopes and intercepts of the NC- and CC-lines, possible deviations of chondrite compositions from their bulk parent body composition is inconsequential.

The CC-line can precisely be determined using the data for carbonaceous chondrites, including the new data for CK, CH, and CB chondrites from this study, and their components. This includes (*i*) chondrule and matrix separates from Allende (CV3)[12], (*ii*) metal, silicate, and chondrule separates from CR2 chondrites[36], (*iii*) acid leachates from Murchison (CM2), Allende (CV3), and Orgueil (CI1)[40,41], and (*iv*) bulk carbonaceous chondrites (CI, CM, CO, CV, CK, CR, CH, CB). A linear regression of this data set yields ε^{95}Mo = (0.596±0.006) × ε^{94}Mo + (0.26±0.02) [MSWD=1.3], consistent with the results in ref. 12. Several iron meteorites (IIC, IID, IIF, IIIF, IVB, and some ungrouped irons) and achondrites (*e.g.*, Eagle Station and Milton pallasites, Tafassasset) also plot on the CC-line; including these samples in the regression yields exactly the same result for the CC-line, but a slightly improved MSWD of 1.1.

The NC-line (Non-Carbonaceous-line) was previously defined as ε^{95}Mo = (0.47±0.14) × ε^{94}Mo – (0.02±0.10), based on data for enstatite and ordinary chondrites as well as some iron meteorites and achondrites[12]. The large uncertainties on both the slope and intercept reflect the limited range of Mo isotope anomalies among these samples, and also the poor precision

of some previous data. A linear regression including (*i*) the new data for bulk NC meteorites from this study (RC, achondrites) together with previously reported data (OC, EC, iron meteorites) and (*ii*) the data for the acid leachates from the ordinary chondrites, yields ε^{95}Mo = (0.596±0.008) × ε^{94}Mo – (0.09±0.02) [MSWD=1.2] (Supplementary Fig. 5). Bulk NC meteorites alone define a less precise correlation line with ε^{95}Mo = (0.530±0.051) × ε^{94}Mo – (0.06±0.04) [MSWD=0.52] with a slightly shallower slope. This slightly different slope suggests that the Mo isotope variations among the NC meteorites are not entirely governed by *s*-process heterogeneity, but that additional small *p*- and/or *r*-process heterogeneities may also exist. However, a regression of only the bulk NC meteorite data with a predefined slope of 0.596 results in an equally good fit (MSWD=0.78). This and the low MSWD of 1.2 for the combined regression (*i.e.*, including bulk meteorites and leachates) demonstrate that the Mo isotope variations among the NC meteorites almost entirely reflect *s*-process variations, and that any additional *p*- and/or *r*-process heterogeneities are minor to absent. The characteristic composition of the NC-line is, therefore, best defined by the combined regression of all data, including the leachates and bulk NC meteorites. Finally, we note that any possible *p*- and/or *r*-process heterogeneity among bulk NC meteorites is small compared to the offset between the NC- and CC-lines (Fig. 1), and is therefore inconsequential for the purpose of using the NC- and CC-lines for reconstructing Earth's accretion history.

With the new Mo isotope data obtained here, both the CC- and NC-lines are now precisely defined. Both lines have an identical slope of 0.596 (in ε^{95}Mo versus ε^{94}Mo space), which is in excellent agreement with a mixing line between terrestrial Mo and a presumed component depleted/enriched in *s*-process Mo as measured in mainstream SiC grains (m ≈ 0.59)[19]. However, the CC- and NC-lines are characterized by significantly different *y*-axis intercepts. The fact that both lines are parallel makes it meaningful to calculate (analogously to the Δ^{17}O notation) a Δ^{95}Mo value for a given sample (see main text), which represents the vertical deviation (in parts-per-million) of a sample from a reference line with ε^{95}Mo = 0.596 × ε^{94}Mo (Supplementary Fig. 1). Note that the *y*-intercept of the CC- and NC-line regressions essentially define the Δ^{95}Mo values of 26±2 and –9±2 (95% CI) for the CC and NC reservoirs, respectively.

S3 Mo isotope composition of bulk silicate Earth

Constraining the relative contributions of NC and CC material to the Earth requires knowledge of the Mo isotope composition of the Earth's mantle. High purity elemental standards are not always good proxies for the mass-independent isotopic composition of the Earth's mantle[21,22], because isotope fractionation induced during production of the standards may not adequately be described by the exponential law, which is conventionally used for correction of instrumental mass fractionation in the isotope measurements. This may lead to small residual anomalies for internally-normalized isotope ratios. For example, several studies have shown that industrially produced steel standards (*e.g.*, NIST SRM 129c and 82b) are affected by mass-dependent Mo isotope fractionation that cannot be described by the exponential law, resulting in anomalous (lower) ε^{i}Mo values relative to the solution standard[14,36,37] (Supplementary Fig. 6). This example highlights that the Mo isotope composition of the bulk silicate Earth (BSE) must be determined by the analyses of terrestrial rock samples.

We analysed a suite of terrestrial rock samples, including different lithologies such as basalts (BCR-2, BHVO-2, JB-2), andesites (JA-2), granodiorites (JG-1), diabases (W-2a), and

dunites (DTS-2b). These samples represent different mantle sources and have highly variable Mo concentrations as well as chemical compositions, and so potential effects of different sample matrices on measured Mo isotope compositions can be ruled out. Of these samples, the USGS reference materials BHVO-2 and, in particular, BCR-2 are heavily contaminated with Mo from steel tools used in the preparation of the sample powders[42]. Consistent with this, the Mo isotope compositions measured for BHVO-2 and BCR-2 slightly deviate from those obtained for the other rock samples, and are shifted towards the compositions measured for the steel standards (Supplementary Fig. 6). As such, BHVO-2 and BCR-2 were not used for the calculation of the BSE composition (Supplementary Table 1).

The other terrestrial rock standards investigated here (JB-2, JA-2, JG-1, W-2a, DTS-2b) have indistinguishable Mo isotope compositions, characterized by a small, albeit systematic, offset (ε^{94}Mo = 0.04±0.06; ε^{95}Mo = 0.10±0.04) from the composition of the Mo solution standard (ε^{i}Mo ≡ 0). A similar offset has also been observed for diamictites and OIBs in a Mo isotope study using thermal ionization mass spectrometry (TIMS)[11], demonstrating that this offset is present for both MC-ICP-MS and TIMS measurements. Therefore, the small offset from zero is not an artefact introduced by a particular measurement method, but is an inherent difference between terrestrial rock samples and the solution standards. As such, this difference most likely results from non-exponential isotopic fractionation (*i.e.*, fractionations that are not accounted for by the mass fractionation correction during the measurements) induced during purification and enrichment of Mo in the production of the solution standard, or during the genesis of the Mo ores from which these standards are produced. The latter would be consistent with the observation that molybdenites have Mo isotope compositions that are closer to those of the solution standards (Supplementary Fig. 6). As such, both the solution standards and the molybdenites do not provide good proxies for the Mo isotope composition of the BSE; this composition is instead best defined by the data for the terrestrial rock samples.

The BSE composition defined by the mean of the analysed rock samples from this study (Supplementary Table 1) is consistent with, albeit much more precise than the composition defined by ref. 11 (ε^{94}Mo = 0.09±0.27; ε^{94}Mo = 0.08±0.15), and plots between the CC- and NC-lines in a diagram of ε^{95}Mo versus ε^{94}Mo (Fig. 2). The Δ^{95}Mo value for the BSE, based on our data, is 7±5 (95% CI, n=5), which is clearly resolved from the values of CC and NC materials. Of note, all individual terrestrial samples analysed in this and previous studies, including steel samples, steel-contaminated rock standards, and solution standards, plot between the CC- and NC-lines. Including such samples in the calculation of the BSE's Δ^{95}Mo would result in a value of 5±4 (95% CI, n=10), which is indistinguishable from the value defined above. Thus, the particular choice of the exact samples used to define the BSE composition has no significant effect on the main conclusion that the Mo isotope composition of the present-day BSE is intermediate between those of the CC and NC materials.

The offset of the BSE's Mo isotopic composition from the NC-line cannot reflect any mass-dependent isotopic fractionation, neither among the analysed terrestrial samples nor between the BSE and Earth's core. All data are corrected for natural and instrumental mass-dependent isotope fractionation, and so the observed isotopic variations are mass-independent in nature. This is confirmed by comparing the isotopic data in diagrams of ε^{95}Mo versus ε^{94}Mo and ε^{95}Mo versus ε^{92}Mo (Supplementary Fig. 2). The former diagram is the classical diagram in which the NC-CC dichotomy is most clearly resolved. However, this dichotomy is also present in the latter diagram, although the difference between the NC- and CC-lines is smaller and analytical uncertainties on ε^{92}Mo are typically larger. First, in the ε^{95}Mo–ε^{94}Mo diagram, any mass-dependent isotope fractionation would follow a slope of ~0.5 [(m^{95}Mo–m^{96}Mo)/(m^{94}Mo–m^{96}Mo)], which is about the same as that of the NC-line (m=0.596); this process, therefore,

cannot cause a significant deviation of the BSE value from the NC-line. Second, in the ε^{95}Mo–ε^{92}Mo diagram, any mass-dependent isotope fractionation would follow a slope of ~0.25 [(m^{95}Mo–m^{96}Mo)/(m^{92}Mo–m^{96}Mo)], which is significantly shallower than that of the NC-line (m=0.483). Thus, in this diagram the position of the BSE could in principle be shifted away from the NC-line by unaccounted mass-dependent fractionation effects. However, in both the ε^{95}Mo–ε^{94}Mo and ε^{95}Mo–ε^{92}Mo diagrams, the BSE plots between the NC- and CC-lines and the relative distances between the BSE and the two lines are the same in both plots. Specifically, the mass fraction of CC-derived Mo (f_{CC}) in the BSE as calculated from the ε^{95}Mo–ε^{94}Mo systematics is 0.46±0.15, and the exact same number (0.46±0.34), albeit with larger uncertainty, is obtained from the ε^{95}Mo–ε^{92}Mo diagram. This consistency demonstrates that the Mo isotopic data are free of any unaccounted mass-dependent effects, because otherwise the ε^{95}Mo–ε^{94}Mo and ε^{95}Mo–ε^{92}Mo systematics would be significantly different. Finally, any mass-dependent Mo isotope fractionation induced during core formation would be very small and—although such a fractionation has been observed experimentally[43]—the temperature of core formation in the Earth was too high to lead to any resolvable mass-dependent Mo isotope fractionation between the BSE and the core[44].

S4 Predicted Δ^{95}Mo of bulk silicate Earth

The Mo present in the bulk silicate Earth (BSE) can be viewed as a mixture of three components: proto-Earth's mantle (*pE*), the giant Moon-forming impactor (*GI*), and the late veneer (*LV*). For the mass balance equations, the following parameters were used:

- *g* = impactor-to-Earth ratio (assumed to be 0.1; *i.e.*, a Mars-sized impactor[23]). For simplicity we assume that all of the impactor mass is accreted by Earth.
- *k* = mass fraction of the Moon-forming impactor core that equilibrated with Earth's mantle; note that this does not include the late veneer, which is the material added after the formation of the Moon and cessation of core formation.
- *f* = mass fraction of the late veneer. This value is obtained from absolute abundances of highly siderophile elements in the bulk silicate Earth, which provides a mass fraction of the late veneer of 0.7±0.2% of the mass of the Earth's mantle[24]. A higher mass fraction of the late veneer is possible if it is assumed that the late veneer consistent of differentiated lunar-sized projectiles, whose core partially merged with Earth's core without prior equilibration with Earth's mantle[45]. However, the Mo contained in the core material that did not equilibrate would not have contributed to the Mo in the present-day BSE. Thus, for estimating the effect of the late veneer on the BSE's Mo isotopic composition, the mass fraction inferred from the abundances of the highly siderophile elements is appropriate.
- γ = mantle mass fraction. A constant value of 0.675 was assumed for both Earth and the impactor.
- *D* = metal-silicate partition coefficient for Mo; this value varies from ~100 to ~1000 depending on various parameters, including pressure, temperature, and oxygen fugacity[46]. However, for the final core formation event in the Earth, which directly followed the giant impact, this value is more precisely defined from the Mo concentration in the BSE compared to that in chondrites, and a D_E value between 100 and 200 has been inferred[46]; here this value is assumed for the final core formation event in the Earth. For core formation in the impactor, the value for D_{GI} is essentially unknown and values between 100 and 1000 were assumed[46].

First, the Mo concentrations in the relevant reservoirs are calculated. The pre-late veneer Mo concentration of the bulk silicate Earth is

$$[Mo]_{pre-LV} = \frac{[Mo]_{BSE} - f[Mo]_{LV}}{1-f}$$

where the Mo concentration of the late veneer is assumed to be chondritic (*i.e.*, 900–1600 ppb[37,47]). For the BSE, a Mo concentration of 23±7 ppb is used[44], indicating that roughly 20–30% of the BSE's Mo derives from the late veneer. The Mo concentration of the giant impactor material that equilibrated with the Mo in the proto-Earth's mantle is

$$[Mo]_{GI} = \frac{\gamma + k(1-\gamma)D_{GI}}{\gamma + (1-\gamma)D_{GI}}[Mo]_{chondrites}$$

where D_{GI} is the metal-silicate partition coefficient appropriate for core formation in the Moon-forming impactor. The Mo concentration of the bulk impactor is assumed to be chondritic. The Mo concentration in proto-Earth's mantle then is

$$[Mo]_{pE} = \frac{[Mo]_{post-GI} - g[Mo]_{GI}}{1-g}$$

where $[Mo]_{post\text{-}GI}$ is the Mo concentration in the silicate Earth after addition of the giant impactor but before segregation of impactor core material to the Earth:

$$[Mo]_{post-GI} = \frac{\gamma + gk(1-g)D_E}{\gamma + gk(1-g)}[Mo]_{pre-LV}$$

The Δ^{95}Mo of the pre-late veneer silicate Earth is then given by

$$\Delta^{95}Mo_{pre-LV} = \frac{(1-g)[Mo]_{pE}\Delta^{95}Mo_{pE} + g[Mo]_{GI}\Delta^{95}Mo_{GI}}{[Mo]_{post-GI}}$$

and the final predicted Δ^{95}Mo of the BSE can be computed as follows:

$$\boldsymbol{\Delta^{95}Mo_{BSE}} = \frac{\boldsymbol{(1-f)[Mo]_{pre-LV}\Delta^{95}Mo_{pre-LV} + f[Mo]_{LV}\Delta^{95}Mo_{LV}}}{\boldsymbol{(1-f)[Mo]_{pre-LV} + f[Mo]_{LV}}}$$

With these governing equations the predicted Δ^{95}Mo of the BSE can be calculated for different assumed Δ^{95}Mo values of the giant impactor, proto-Earth's mantle and the late veneer. The uncertainties on all parameters were propagated by a Monte Carlo simulation, where all parameters were varied randomly within their given bounds as given above, and values for *k* were varied randomly between 0 (no equilibration) and 1 (full equilibration). The calculations were performed for several distinct sets of assumed compositions of the giant impactor, proto-Earth's mantle and the late veneer, including different combinations of pure CC (Δ^{95}Mo = +26±2), pure NC (Δ^{95}Mo = –9±2), and mixed NC-CC compositions. For simplicity, the mixed NC-CC compositions were assumed to be within the range of the observed Δ^{95}Mo

for the BSE (Δ^{95}Mo = +7±5). The results of the calculations are plotted in Fig. 3, where the dots in each panel represent the outcome of the Monte Carlo simulation with N≈30,000.

For each set of assumed compositions for the giant impactor, proto-Earth's mantle, and the late veneer, the results of the calculations are translated into probabilities to match the BSE's Δ^{95}Mo by comparing the number of solutions matching the BSE's Δ^{95}Mo of 7±5 to the total number of solutions. This comparison is done in steps of *k* of 0.02, so that for each step a probability is obtained. The resulting probabilities are plotted in Fig. 4 as a function of the degree of impactor core re-equilibration (*k*).

S5 Supplementary Figures and Tables

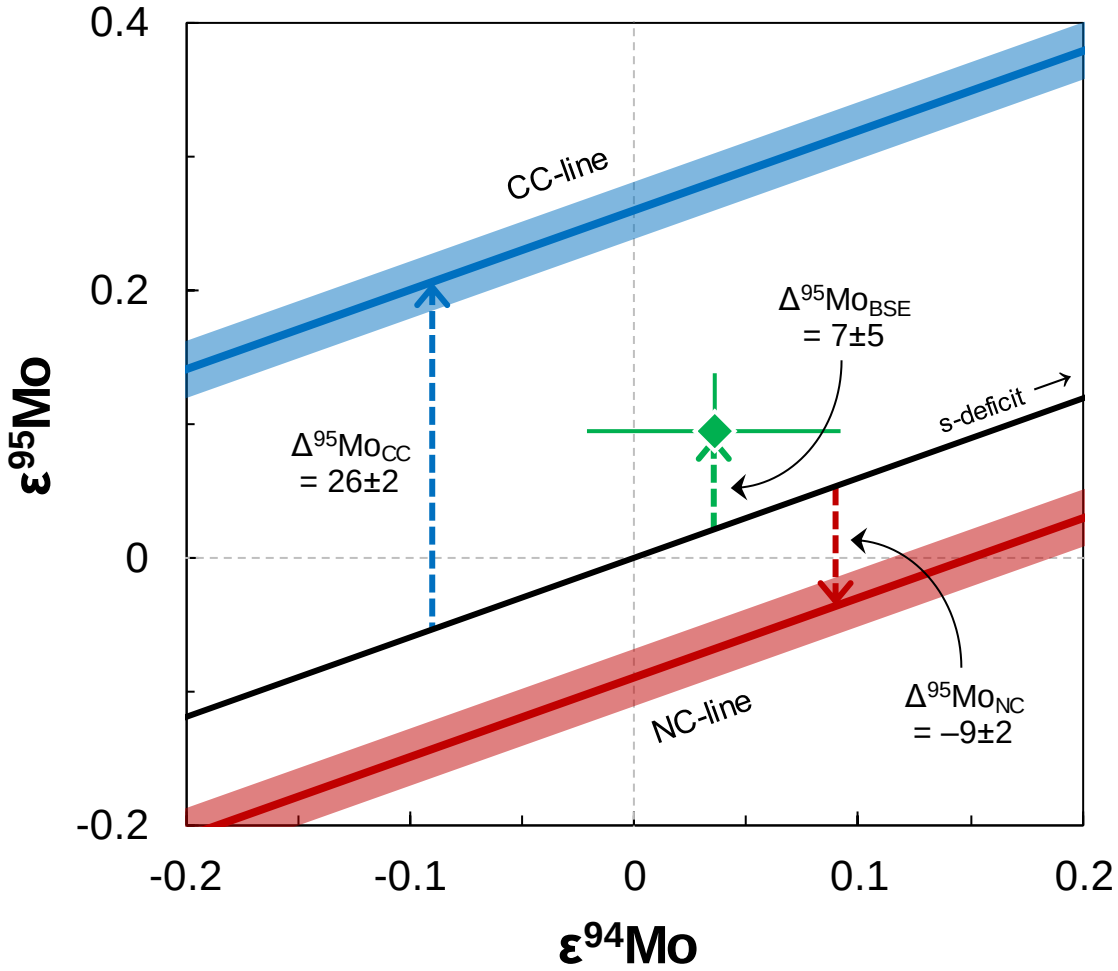

Supplementary Figure 1. Schematic diagram of ε^{95}Mo versus ε^{94}Mo. Solid black line is an *s*-process mixing line passing through zero (*i.e.*, the composition of the Mo standard). Δ^{95}Mo represents the vertical deviation (in parts-per-million) of a given sample from this reference line. Irrespective of the absolute isotope anomaly, CC and NC samples are characterized by distinct Δ^{95}Mo, while the BSE has an intermediate value. Error envelopes represent 95% confidence intervals (95% CI) of the CC- and NC-line regressions (see Section S2 for details).

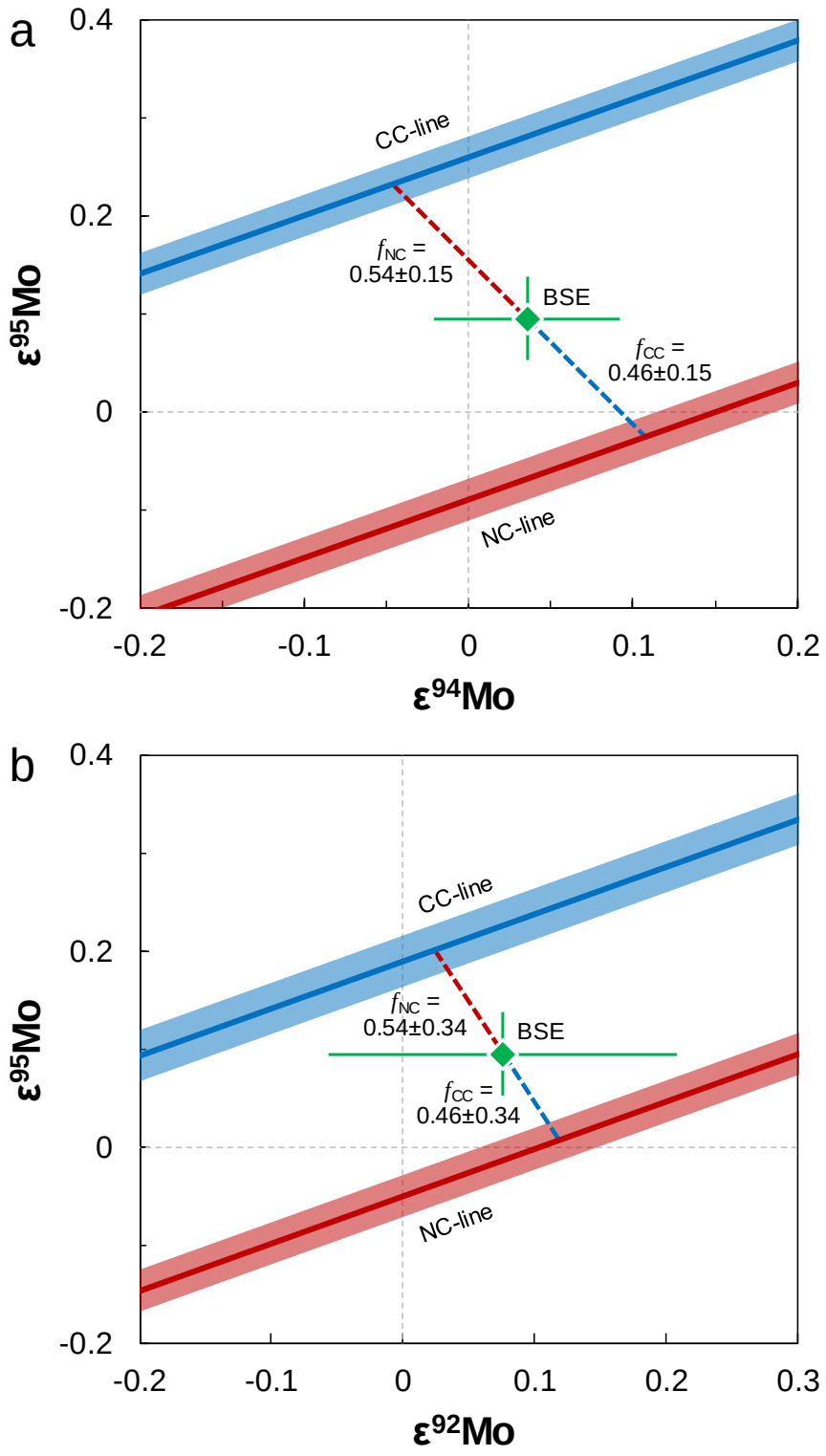

Supplementary Figure 2. Diagrams of ε^{95}Mo versus ε^{94}Mo (a) and ε^{92}Mo (b). In both diagrams, carbonaceous (CC, blue) and non-carbonaceous (NC, red) meteorites define two parallel lines. Hence, the BSE composition divides any tie line between the NC- and CC-lines into two segments whose ratio to each other is constant (examples shown here). This allows quantifying the relative contributions of NC and CC material regardless of the position of the endmembers on the lines, which are the same in both diagrams. Note that in the ε^{95}Mo–ε^{92}Mo diagram (b) the uncertainties are generally larger, and the CC- and NC-lines are ε^{95}Mo = (0.482±0.005) × ε^{92}Mo + (0.19±0.03) and ε^{95}Mo = (0.483±0.008) × ε^{92}Mo – (0.05±0.02), respectively (calculated as described in Section S2 for the ε^{95}Mo–ε^{94}Mo diagram).

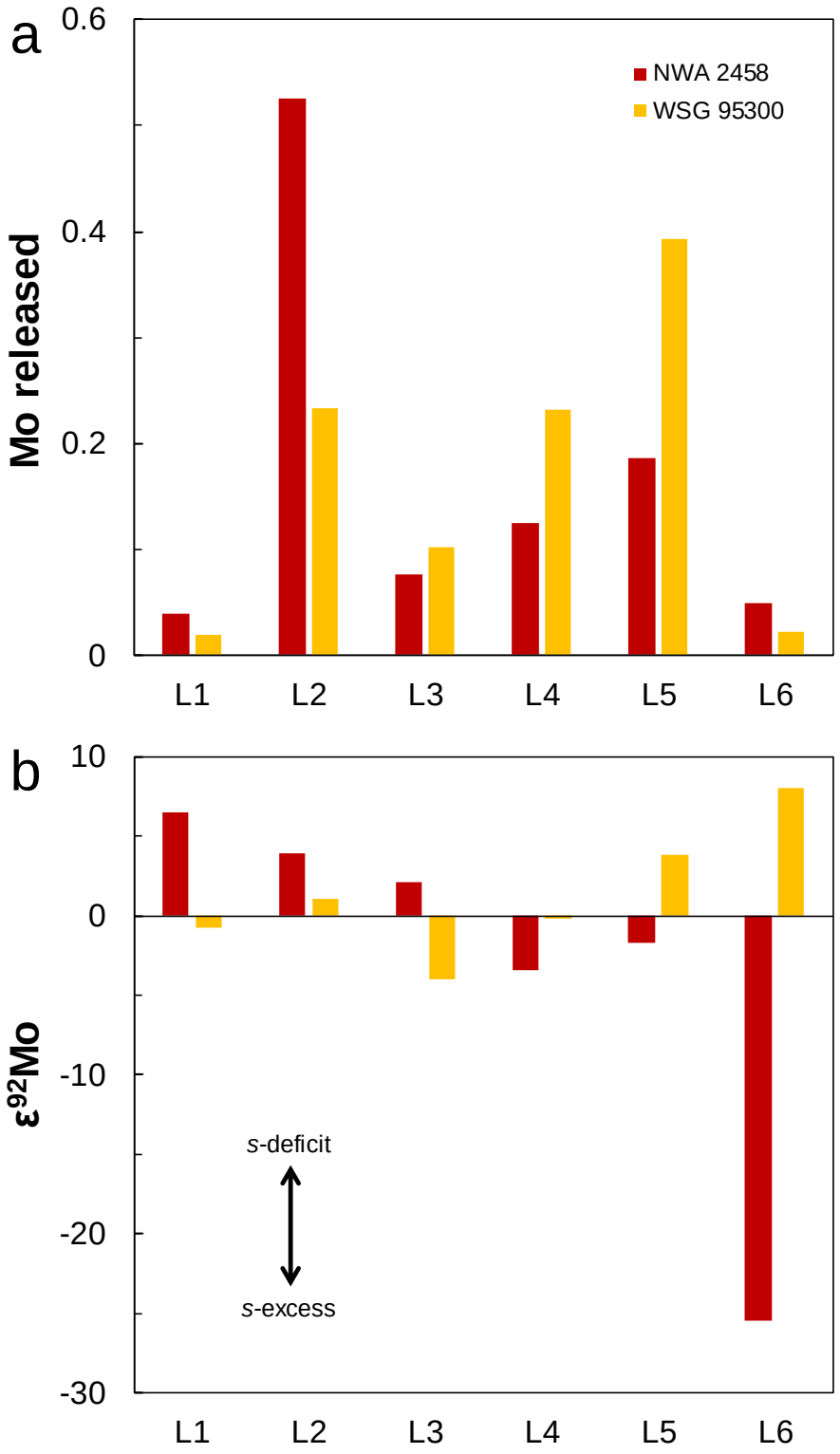

Supplementary Figure 3. Fraction of Mo released (a) and ε^{92}Mo (b) for the different leaching steps. The two unequilibrated ordinary chondrites NWA 2458 (L3.2) and WSG 95300 (H3.3) show distinct elemental and isotopic patterns.

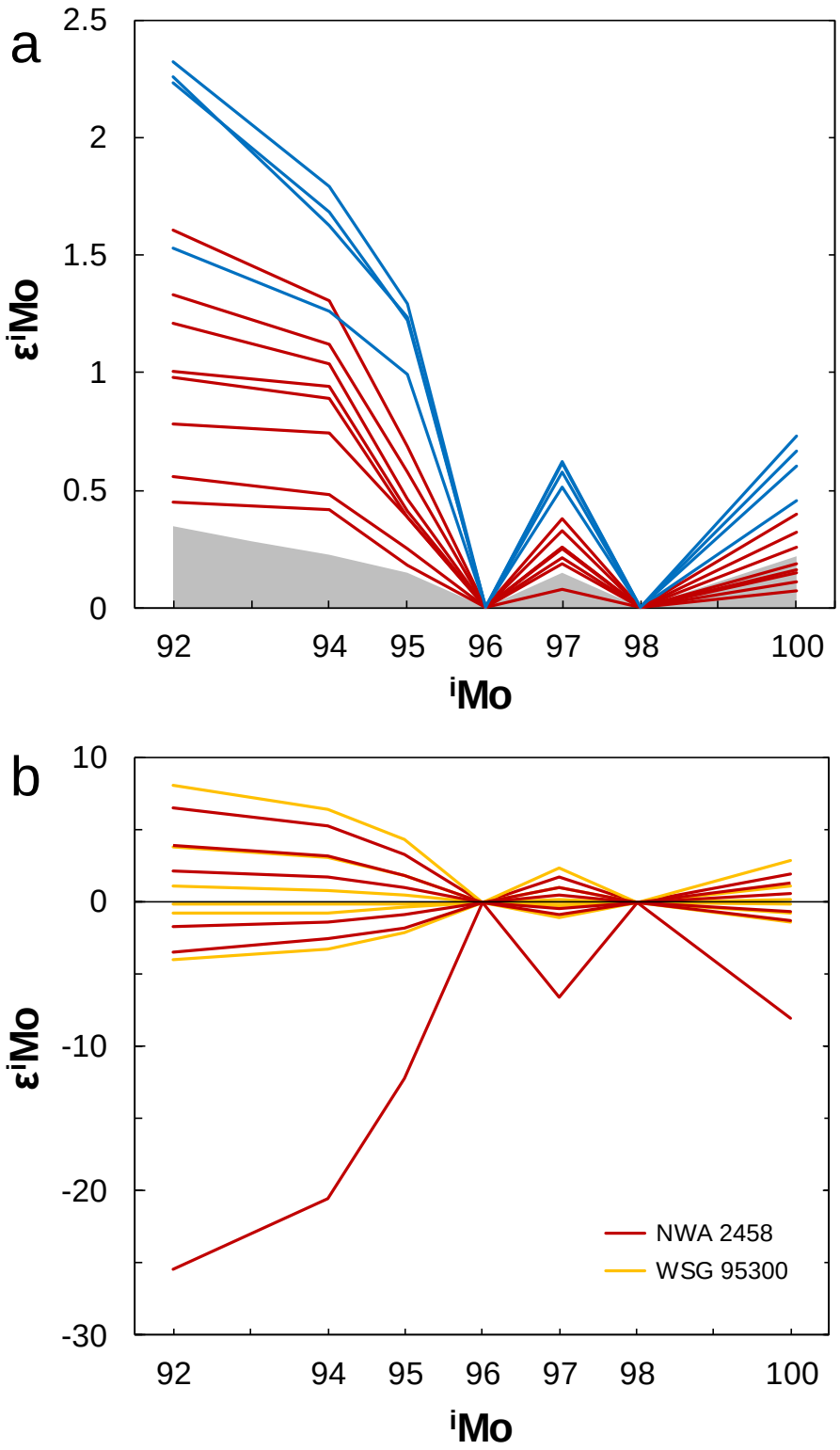

Supplementary Figure 4. Molybdenum isotope patterns of bulk meteorites (a) and acid leachates (b) from this study. All samples exhibit the typical *w*-shaped (or *m*-shaped) Mo isotope pattern indicative of a deficit (or excess) in *s*-process Mo nuclides.

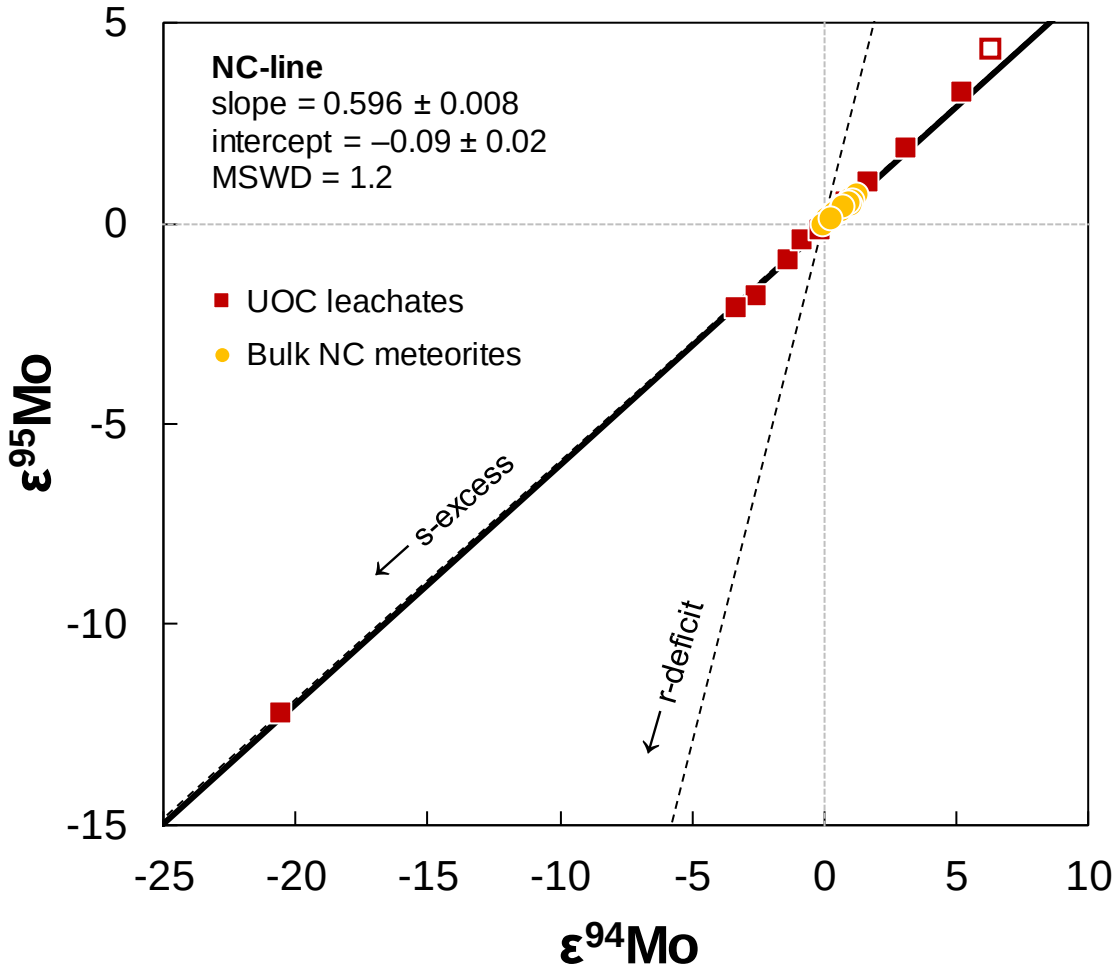

Supplementary Figure 5. Diagram of ε^{95}Mo versus ε^{94}Mo showing the combined regression of bulk (NC) meteorites and acid leachates from unequilibrated ordinary chondrites (NWA 2458, WSG 95300). This NC-line has a slope that is in excellent agreement with the predicted slope for *s*-process variability and a resolved negative *y*-axis intercept. Leachate step L6 from WSG 95300 (open symbol) was excluded from the regression (see Section S1).

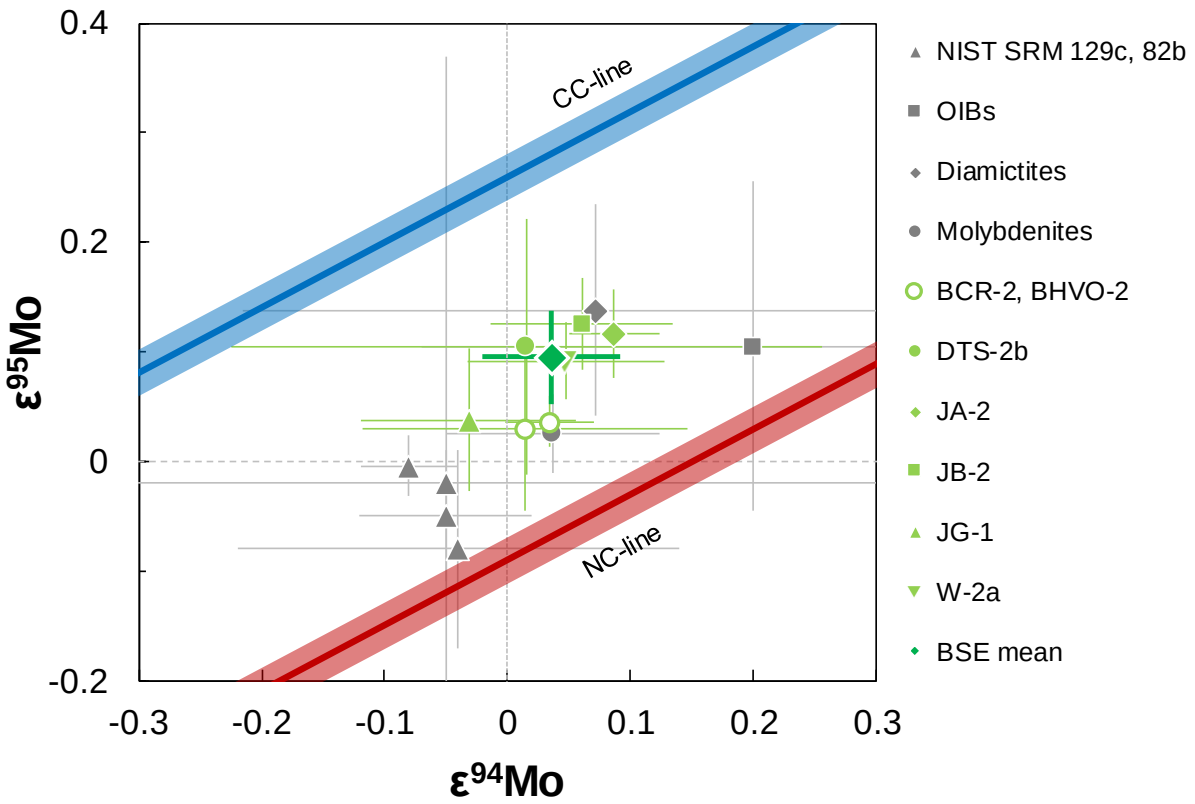

Supplementary Figure 6. Diagram of ε^{95}Mo versus ε^{94}Mo showing terrestrial samples relative to the CC- and NC-lines. Green symbols represent data from this study, grey symbols are literature data. Relative to the Mo solution standard (ε^{i}Mo ≡ 0), steel standards (NIST SRM 129c and 82b)[14,36,37] show slightly negative ε^{94}Mo and ε^{95}Mo. In contrast, the terrestrial rock standards analysed here (DTS-2b, JA-2, JB-2, JG-1, W-2a) as well as OIBs and diamictites from a previous study[11] show positive values. The (steel-contaminated) rock standards BHVO-2 and BCR-2 (open symbols) as well as molybdenites[11] plot closest to the solution standard. See Section S3 for details. Error bars typically represent 95% confidence intervals (95% CI).

Supplementary Table 1. Mo isotope data for meteoritic and terrestrial samples.

Sample		Weight (g)	Mo (µg/g)	N	ε^{92}Mo	ε^{94}Mo	ε^{95}Mo	ε^{97}Mo	ε^{100}Mo
Unprocessed solution standards									
Alfa Aesar (bracketing standard)		–	–		≡ 0	≡ 0	≡ 0	≡ 0	≡ 0
NIST SRM 3134		–	–	42	-0.04 ± 0.05	0.00 ± 0.04	0.01 ± 0.03	0.02 ± 0.02	-0.01 ± 0.03
Alfa Aesar Specpure Plasma		–	–	24	0.04 ± 0.10	0.04 ± 0.05	0.02 ± 0.04	0.00 ± 0.03	-0.01 ± 0.06
Processed solution standards									
Alfa Aesar (bracketing standard)		–	–	10	0.00 ± 0.15	-0.01 ± 0.11	0.03 ± 0.07	0.06 ± 0.03	0.00 ± 0.08
NIST SRM 3134		–	–	10	-0.02 ± 0.17	0.02 ± 0.11	0.05 ± 0.05	0.03 ± 0.06	-0.07 ± 0.07
Alfa Aesar (with DTS-2b matrix)		–	–	14	-0.01 ± 0.10	0.00 ± 0.06	0.03 ± 0.04	0.02 ± 0.05	-0.04 ± 0.04
Terrestrial rock samples									
BHVO-2	*OIB*	–	*4.07*	*40*	*0.01 ± 0.06*	*0.03 ± 0.04*	*0.04 ± 0.02*	*0.01 ± 0.02*	*-0.08 ± 0.04*
BCR-2	*Cont. flood basalt*	–	*250.6*	*10*	*-0.11 ± 0.14*	*0.01 ± 0.13*	*0.03 ± 0.07*	*0.02 ± 0.04*	*-0.08 ± 0.10*
JB-2	Arc basalt	–	1.014	15	0.11 ± 0.09	0.06 ± 0.07	0.13 ± 0.04	0.08 ± 0.04	-0.09 ± 0.05
JA-2	Andesite	–	0.581	17	0.17 ± 0.07	0.09 ± 0.04	0.12 ± 0.04	0.04 ± 0.04	-0.03 ± 0.07
JG-1	Granodiorite	–	1.54	7	-0.10 ± 0.12	-0.03 ± 0.09	0.04 ± 0.07	0.07 ± 0.05	-0.05 ± 0.09
W-2a	Diabase	–	0.465	10	0.08 ± 0.12	0.05 ± 0.08	0.09 ± 0.04	0.05 ± 0.03	-0.08 ± 0.06
DTS-2b	Dunite	–	0.057	4	0.13 ± 0.38	0.02 ± 0.24	0.10 ± 0.12	0.06 ± 0.09	-0.08 ± 0.31
Bulk silicate Earth	*(±95% CI)*	–	–	–	*0.08 ± 0.13*	*0.04 ± 0.06*	*0.10 ± 0.04*	*0.06 ± 0.02*	*-0.07 ± 0.04*
Bulk meteorites									
CK chondrites	NWA 6604	0.556	0.45	3	2.26 ± 0.35	1.63 ± 0.22	1.24 ± 0.15	0.58 ± 0.15	0.73 ± 0.22
CH chondrites	Acfer 182	0.553	1.60	6	2.32 ± 0.11	1.79 ± 0.10	1.29 ± 0.04	0.62 ± 0.09	0.66 ± 0.11
CB chondrites	HaH 237	0.561	3.23	9	1.53 ± 0.08	1.26 ± 0.04	0.99 ± 0.04	0.51 ± 0.04	0.45 ± 0.04
Rumuruti chondrites	NWA 053	0.564	0.92	4	0.35 ± 0.18	0.33 ± 0.12	0.15 ± 0.06	0.06 ± 0.06	0.07 ± 0.19
	NWA 753	0.559	0.57	3	0.72 ± 0.35	0.65 ± 0.22	0.31 ± 0.15	0.19 ± 0.15	0.17 ± 0.22
	NWA 6145	0.450	0.72	3	0.53 ± 0.35	0.49 ± 0.22	0.23 ± 0.15	0.09 ± 0.15	0.12 ± 0.22
	Weighted Average	–	–	–	*0.45 ± 0.15*	*0.42 ± 0.10*	*0.18 ± 0.05*	*0.08 ± 0.05*	*0.11 ± 0.12*
Acapulcoites	Dho 125	0.535	0.91	5	1.01 ± 0.24	0.94 ± 0.12	0.41 ± 0.07	0.26 ± 0.08	0.26 ± 0.11
Brachinites	NWA 3151	0.531	0.47	3	1.29 ± 0.35	1.14 ± 0.22	0.61 ± 0.15	0.36 ± 0.15	0.38 ± 0.22
	NWA 4882	1.102	0.38	4	1.34 ± 0.16	1.10 ± 0.21	0.56 ± 0.11	0.32 ± 0.04	0.31 ± 0.10
	Weighted Average	–	–	–	*1.33 ± 0.15*	*1.12 ± 0.15*	*0.58 ± 0.08*	*0.33 ± 0.04*	*0.32 ± 0.09*
Ureilites	Dho 1519	0.820	0.76	4	0.64 ± 0.19	0.61 ± 0.14	0.32 ± 0.10	0.22 ± 0.08	0.03 ± 0.12
	NWA 7630	0.798	0.53	3	1.06 ± 0.35	1.01 ± 0.22	0.44 ± 0.15	0.26 ± 0.15	0.26 ± 0.22
	ALHA 77257	1.240	0.22	2	0.74 ± 0.35	0.79 ± 0.22	0.26 ± 0.15	0.15 ± 0.15	0.00 ± 0.22
	EET 87720	1.236	0.12	1	1.02 ± 0.35	0.79 ± 0.22	0.38 ± 0.15	0.23 ± 0.15	0.35 ± 0.22
	EET 96042	0.759	0.39	2	1.14 ± 0.35	1.10 ± 0.22	0.42 ± 0.15	0.21 ± 0.15	0.19 ± 0.22
	GRA 95205	0.877	0.48	3	1.15 ± 0.35	1.00 ± 0.22	0.43 ± 0.15	0.32 ± 0.15	0.28 ± 0.22
	LAP 03721	1.253	0.20	1	0.91 ± 0.35	0.87 ± 0.22	0.37 ± 0.15	0.13 ± 0.15	0.10 ± 0.22
	LAR 04315	1.234	0.29	2	1.12 ± 0.35	0.99 ± 0.22	0.34 ± 0.15	0.14 ± 0.15	0.22 ± 0.22
	MIL 090031	1.118	0.30	3	1.18 ± 0.35	1.05 ± 0.22	0.45 ± 0.15	0.25 ± 0.15	0.20 ± 0.22
	GRO 95575	1.275	0.16	1	1.17 ± 0.35	1.07 ± 0.22	0.47 ± 0.15	0.30 ± 0.15	0.21 ± 0.22
	NWA 3140	0.512	0.30	1	0.98 ± 0.35	0.86 ± 0.22	0.42 ± 0.15	0.23 ± 0.15	-0.09 ± 0.22
	NWA 3156	0.676	0.32	1	0.83 ± 0.35	0.72 ± 0.22	0.24 ± 0.15	0.23 ± 0.15	0.07 ± 0.22
	NWA 7276	1.284	0.24	2	0.65 ± 0.35	0.68 ± 0.22	0.29 ± 0.15	0.16 ± 0.15	0.00 ± 0.22
	Dho 132	1.437	0.34	3	0.66 ± 0.35	0.65 ± 0.22	0.35 ± 0.15	0.22 ± 0.15	0.11 ± 0.22
	MS-MU-17	0.930	0.13	1	1.08 ± 0.35	0.93 ± 0.22	0.42 ± 0.15	0.13 ± 0.15	0.30 ± 0.22
	MS-MU-20	0.963	0.32	2	1.40 ± 0.35	1.15 ± 0.22	0.51 ± 0.15	0.25 ± 0.15	0.20 ± 0.22
	EET 87517	*1.091*	*0.38*	*2*	*1.90 ± 0.35*	*1.62 ± 0.22*	*0.83 ± 0.15*	*0.48 ± 0.15*	*0.47 ± 0.22*
	PCA 82506	*1.081*	*0.21*	*1*	*2.04 ± 0.35*	*1.35 ± 0.22*	*0.73 ± 0.15*	*0.30 ± 0.15*	*0.40 ± 0.22*
	Weighted Average	–	–	–	*0.98 ± 0.12*	*0.89 ± 0.09*	*0.38 ± 0.04*	*0.21 ± 0.03*	*0.15 ± 0.07*
Mesosiderites	Acfer 063	0.399	2.37	6	1.23 ± 0.21	1.05 ± 0.12	0.46 ± 0.07	0.26 ± 0.04	0.21 ± 0.09
	Ilafegh 002	0.336	2.43	7	1.16 ± 0.23	1.01 ± 0.16	0.45 ± 0.12	0.26 ± 0.08	0.18 ± 0.05
	NWA 2538	0.328	1.81	5	1.27 ± 0.34	1.04 ± 0.17	0.49 ± 0.12	0.24 ± 0.06	0.23 ± 0.14
	Weighted Average	–	–	–	*1.21 ± 0.14*	*1.04 ± 0.08*	*0.46 ± 0.05*	*0.25 ± 0.03*	*0.19 ± 0.04*
Angrites	NWA 4931	2.210	0.31	5	0.78 ± 0.28	0.75 ± 0.11	0.39 ± 0.06	0.26 ± 0.10	0.07 ± 0.12
Aubrites	Peña Blanca Spring	10.50	0.01	1	0.50 ± 0.35	0.58 ± 0.22	0.16 ± 0.15	0.07 ± 0.15	0.16 ± 0.22
	Norton County (metal)	0.501	2.85	6	0.57 ± 0.14	0.47 ± 0.05	0.26 ± 0.06	0.19 ± 0.03	0.17 ± 0.11
	Weighted Average	–	–	–	*0.56 ± 0.13*	*0.48 ± 0.05*	*0.25 ± 0.06*	*0.19 ± 0.03*	*0.16 ± 0.10*
Tafassasset (metal)	(ungr. achondrite)	0.418	8.25	7	2.17 ± 0.15	1.65 ± 0.07	1.20 ± 0.05	0.62 ± 0.05	0.63 ± 0.06
NWA 1058	(ungr. achondrite)	0.514	1.41	6	1.61 ± 0.12	1.31 ± 0.11	0.68 ± 0.09	0.38 ± 0.10	0.40 ± 0.08

Supplementary Table 1. *Continued*.

Sample		Weight (g)	Mo (µg/g)	N	ε^{92}Mo	ε^{94}Mo	ε^{95}Mo	ε^{97}Mo	ε^{100}Mo
Acid leachates									
NWA 2458	L1	–	(156)	1	6.47 ± 0.35	5.30 ± 0.22	3.25 ± 0.15	1.76 ± 0.15	1.93 ± 0.22
(L3.2)	L2	–	(2078)	6	3.90 ± 0.20	3.18 ± 0.08	1.87 ± 0.09	0.98 ± 0.05	1.28 ± 0.07
	L3	–	(301)	2	2.13 ± 0.35	1.70 ± 0.22	1.00 ± 0.15	0.53 ± 0.15	0.55 ± 0.22
	L4	–	(495)	4	-3.45 ± 0.31	-2.57 ± 0.28	-1.82 ± 0.15	-0.90 ± 0.07	-1.24 ± 0.07
	L5	–	(737)	5	-1.69 ± 0.36	-1.36 ± 0.24	-0.89 ± 0.14	-0.50 ± 0.04	-0.71 ± 0.07
	L6	–	(192)	2	-25.43 ± 0.35	-20.53 ± 0.22	-12.22 ± 0.15	-6.55 ± 0.15	-8.04 ± 0.22
	Total / Wtd. Average	–	*(3958)*	–	*0.49*	*0.44*	*0.20*	*0.10*	*0.11*
	Whole rock	0.668	0.67	4	0.42 ± 0.32	0.37 ± 0.28	0.21 ± 0.17	0.16 ± 0.07	0.02 ± 0.09
WSG 95300	L1	–	(98)	1	-0.74 ± 0.35	-0.76 ± 0.22	-0.40 ± 0.15	-0.27 ± 0.15	-0.74 ± 0.22
(H3.3)	L2	–	(1198)	4	1.10 ± 0.04	0.83 ± 0.13	0.52 ± 0.04	0.21 ± 0.07	0.16 ± 0.09
	L3	–	(523)	4	-4.03 ± 0.36	-3.30 ± 0.24	-2.10 ± 0.15	-1.12 ± 0.07	-1.39 ± 0.15
	L4	–	(1187)	6	-0.15 ± 0.24	-0.10 ± 0.14	-0.17 ± 0.12	-0.02 ± 0.07	-0.19 ± 0.17
	L5	–	(2021)	6	3.81 ± 0.14	3.13 ± 0.11	1.89 ± 0.10	0.98 ± 0.10	1.09 ± 0.11
	L6	–	(109)	1	8.09 ± 0.35	6.40 ± 0.22	4.32 ± 0.15	2.37 ± 0.15	2.88 ± 0.22
	Total / Wtd. Average	–	*(5137)*	–	*1.47*	*1.19*	*0.69*	*0.36*	*0.33*

Mo isotope ratios are normalized to ^{98}Mo/^{96}Mo = 1.453173 and reported relative to the Alfa Aesar bracketing standard. Given uncertainties represent the external reproducibility (2 s.d.) obtained from repeated analyses of BHVO-2 (Supplementary Table 2) or 95% confidence intervals (95% CI) for samples with N>3 (N: number of analyses). BHVO-2 and BCR-2 are not included in the BSE mean (see Section S3); EET 87517 and PCA 82506 are distinct from other ureilites and thus not included in the group mean. Mo concentrations were determined by quadrupole ICP-MS, which have an uncertainty of ~5%; values for rock standards are from GeoReM database; for acid leachates the amount of Mo (ng) released in the respective step is reported (values in parentheses).

Supplementary Table 2. Mo isotope data for terrestrial rock standards.

Sample / ID	ε^{92}Mo (± 2 s.e.)	ε^{94}Mo (± 2 s.e.)	ε^{95}Mo (± 2 s.e.)	ε^{97}Mo (± 2 s.e.)	ε^{100}Mo (± 2 s.e.)
BHVO-2					
BHV22.1	-0.34 ± 0.19	-0.08 ± 0.13	-0.03 ± 0.10	-0.02 ± 0.08	-0.06 ± 0.12
BHV22.2	0.25 ± 0.23	0.17 ± 0.17	0.02 ± 0.12	0.00 ± 0.08	-0.02 ± 0.14
BHV22.3	-0.13 ± 0.22	-0.05 ± 0.15	0.02 ± 0.11	0.08 ± 0.09	-0.02 ± 0.13
BHV22.4	0.06 ± 0.20	0.08 ± 0.17	-0.03 ± 0.11	-0.10 ± 0.09	-0.08 ± 0.13
BHV22.5	-0.06 ± 0.20	-0.11 ± 0.12	0.02 ± 0.10	0.01 ± 0.07	-0.24 ± 0.11
BHV22.6	0.21 ± 0.18	0.13 ± 0.13	0.11 ± 0.09	0.03 ± 0.09	-0.19 ± 0.12
BHV22.7	-0.11 ± 0.22	0.03 ± 0.15	-0.02 ± 0.12	-0.05 ± 0.08	-0.12 ± 0.14
BHV22.8	0.01 ± 0.21	0.12 ± 0.15	0.01 ± 0.11	0.06 ± 0.09	-0.06 ± 0.12
BHV23.1	-0.09 ± 0.22	0.14 ± 0.13	0.02 ± 0.09	0.01 ± 0.08	-0.01 ± 0.14
BHV23.2	0.22 ± 0.22	0.14 ± 0.15	0.08 ± 0.10	0.05 ± 0.07	-0.30 ± 0.13
BHV23.3	0.32 ± 0.19	0.10 ± 0.15	0.05 ± 0.09	-0.06 ± 0.09	-0.19 ± 0.11
BHV23.4	0.04 ± 0.20	-0.01 ± 0.15	0.00 ± 0.12	-0.12 ± 0.09	-0.26 ± 0.13
BHV23.5	-0.10 ± 0.18	-0.04 ± 0.13	0.03 ± 0.09	0.02 ± 0.08	-0.12 ± 0.12
BHV23.6	-0.08 ± 0.20	-0.01 ± 0.14	0.02 ± 0.09	0.04 ± 0.07	-0.05 ± 0.11
BHV23.7	-0.04 ± 0.23	0.04 ± 0.15	0.06 ± 0.12	-0.05 ± 0.08	-0.17 ± 0.13
BHV23.8	0.05 ± 0.19	0.12 ± 0.13	0.08 ± 0.09	0.06 ± 0.08	0.08 ± 0.13
BHV24.1	-0.02 ± 0.15	0.13 ± 0.10	0.05 ± 0.08	0.05 ± 0.07	-0.24 ± 0.11
BHV24.2	-0.12 ± 0.21	-0.04 ± 0.13	-0.05 ± 0.11	-0.07 ± 0.07	0.03 ± 0.13
BHV24.3	-0.08 ± 0.20	-0.14 ± 0.13	-0.01 ± 0.10	-0.14 ± 0.09	0.08 ± 0.10
BHV24.4	0.13 ± 0.22	0.03 ± 0.14	0.11 ± 0.11	0.03 ± 0.07	-0.16 ± 0.14
BHV24.5	0.01 ± 0.16	0.03 ± 0.12	0.07 ± 0.09	-0.09 ± 0.08	-0.03 ± 0.12
BHV24.6	0.13 ± 0.21	0.07 ± 0.14	0.09 ± 0.11	0.01 ± 0.09	-0.19 ± 0.13
BHV24.7	0.01 ± 0.18	0.07 ± 0.14	0.10 ± 0.10	0.09 ± 0.08	-0.14 ± 0.12
BHV24.8	-0.09 ± 0.20	-0.13 ± 0.13	-0.03 ± 0.10	0.13 ± 0.09	-0.06 ± 0.12
BHV25.1	0.27 ± 0.18	0.27 ± 0.13	0.13 ± 0.09	0.03 ± 0.07	-0.13 ± 0.10
BHV25.2	0.27 ± 0.19	0.01 ± 0.13	0.10 ± 0.10	-0.09 ± 0.08	-0.15 ± 0.12
BHV25.3	-0.27 ± 0.18	-0.06 ± 0.13	-0.10 ± 0.09	-0.02 ± 0.08	0.16 ± 0.12
BHV25.4	0.02 ± 0.20	0.07 ± 0.14	0.15 ± 0.10	0.10 ± 0.08	0.01 ± 0.14
BHV25.5	0.22 ± 0.19	0.21 ± 0.14	0.13 ± 0.10	-0.10 ± 0.09	-0.05 ± 0.11
BHV25.6	-0.30 ± 0.21	-0.13 ± 0.14	-0.03 ± 0.10	0.00 ± 0.08	0.09 ± 0.13
BHV25.7	-0.05 ± 0.21	-0.03 ± 0.14	0.02 ± 0.10	0.10 ± 0.08	-0.04 ± 0.11
BHV25.8	-0.04 ± 0.17	-0.04 ± 0.13	-0.05 ± 0.09	0.09 ± 0.06	0.01 ± 0.13
BHV26.10	-0.24 ± 0.22	-0.07 ± 0.14	-0.09 ± 0.11	0.00 ± 0.07	0.00 ± 0.12
BHV26.11	0.04 ± 0.19	0.04 ± 0.13	-0.04 ± 0.09	-0.03 ± 0.07	-0.22 ± 0.12
BHV26.12	0.08 ± 0.23	0.14 ± 0.14	0.11 ± 0.12	-0.08 ± 0.08	-0.10 ± 0.12
BHV26.13	0.12 ± 0.20	0.08 ± 0.15	0.08 ± 0.11	-0.01 ± 0.09	-0.09 ± 0.12
BHV26.14	-0.04 ± 0.21	-0.07 ± 0.14	-0.04 ± 0.10	0.06 ± 0.09	-0.09 ± 0.12
BHV26.15	0.22 ± 0.18	0.08 ± 0.14	0.23 ± 0.10	0.16 ± 0.09	0.03 ± 0.12
BHV26.16	0.25 ± 0.21	0.27 ± 0.13	0.11 ± 0.10	0.17 ± 0.09	-0.14 ± 0.12
BHV26.17	-0.35 ± 0.20	-0.22 ± 0.17	-0.05 ± 0.12	0.01 ± 0.09	0.13 ± 0.13
N	40	40	40	40	40
Mean	0.01	0.03	0.04	0.01	-0.08
2 s.d.	0.35	0.22	0.15	0.15	0.22
95% CI	0.06	0.04	0.02	0.02	0.04
BCR-2					
BCR_A.1	-0.15 ± 0.24	-0.02 ± 0.17	-0.07 ± 0.11	-0.05 ± 0.08	-0.04 ± 0.15
BCR_A.2	-0.32 ± 0.19	-0.15 ± 0.16	-0.05 ± 0.10	-0.07 ± 0.08	0.05 ± 0.12
BCR_A.3	0.14 ± 0.20	0.13 ± 0.14	0.18 ± 0.09	0.01 ± 0.09	-0.12 ± 0.13
BCR_A.4	-0.32 ± 0.22	-0.23 ± 0.15	-0.15 ± 0.11	0.03 ± 0.10	0.00 ± 0.13
BCR_A.5	-0.13 ± 0.20	-0.09 ± 0.13	0.01 ± 0.11	0.00 ± 0.08	-0.16 ± 0.14
BCR_A.6	0.06 ± 0.21	0.21 ± 0.15	0.14 ± 0.09	0.06 ± 0.07	-0.23 ± 0.13
BCR_A.7	0.05 ± 0.19	0.33 ± 0.14	0.10 ± 0.10	0.00 ± 0.08	-0.24 ± 0.12
BCR_A.8	0.03 ± 0.20	0.17 ± 0.15	0.09 ± 0.12	0.04 ± 0.08	0.05 ± 0.12
BCR_A.9	-0.46 ± 0.20	-0.18 ± 0.15	-0.02 ± 0.10	0.14 ± 0.08	0.12 ± 0.12
BCR_A.10	0.01 ± 0.18	-0.04 ± 0.13	0.07 ± 0.10	0.04 ± 0.09	-0.28 ± 0.13
DTS-2b					
DTS39	0.26 ± 0.24	0.04 ± 0.16	0.10 ± 0.11	0.06 ± 0.08	-0.30 ± 0.15
DTS44.1	-0.06 ± 0.22	-0.18 ± 0.15	0.05 ± 0.11	0.00 ± 0.09	0.17 ± 0.16
DTS44.2	0.40 ± 0.25	0.19 ± 0.17	0.21 ± 0.11	0.03 ± 0.11	-0.14 ± 0.14
DTS44.3	-0.08 ± 0.24	0.01 ± 0.15	0.05 ± 0.11	0.14 ± 0.08	-0.06 ± 0.15

Supplementary Table 2. *Continued*.

Sample / ID	ε^{92}Mo (± 2 s.e.)	ε^{94}Mo (± 2 s.e.)	ε^{95}Mo (± 2 s.e.)	ε^{97}Mo (± 2 s.e.)	ε^{100}Mo (± 2 s.e.)
JB-2					
JB201.1	-0.04 ± 0.18	0.12 ± 0.11	0.08 ± 0.10	0.06 ± 0.07	0.00 ± 0.13
JB201.2	0.21 ± 0.20	0.27 ± 0.15	0.23 ± 0.09	0.14 ± 0.08	-0.16 ± 0.13
JB201.3	0.42 ± 0.18	0.26 ± 0.14	0.21 ± 0.09	0.14 ± 0.08	-0.27 ± 0.12
JB201.4	-0.15 ± 0.20	-0.18 ± 0.14	0.09 ± 0.10	0.01 ± 0.08	-0.08 ± 0.14
JB201.5	0.02 ± 0.21	-0.01 ± 0.14	0.10 ± 0.10	0.05 ± 0.08	0.02 ± 0.13
JB201.6	0.01 ± 0.21	0.06 ± 0.16	0.14 ± 0.11	0.16 ± 0.08	0.00 ± 0.13
JB201.7	0.18 ± 0.19	0.00 ± 0.13	0.12 ± 0.10	0.03 ± 0.08	-0.03 ± 0.14
JB202.1	0.06 ± 0.17	-0.04 ± 0.12	0.13 ± 0.09	0.03 ± 0.08	-0.13 ± 0.13
JB202.2	0.27 ± 0.21	0.05 ± 0.17	0.29 ± 0.10	0.16 ± 0.08	-0.18 ± 0.12
JB202.3	0.07 ± 0.21	0.14 ± 0.12	0.07 ± 0.11	0.18 ± 0.09	-0.15 ± 0.12
JB202.4	0.07 ± 0.20	-0.02 ± 0.15	0.15 ± 0.10	0.03 ± 0.08	-0.09 ± 0.12
JB204.1	0.03 ± 0.23	-0.02 ± 0.17	-0.01 ± 0.11	-0.03 ± 0.07	0.00 ± 0.12
JB204.2	0.38 ± 0.22	0.26 ± 0.16	0.16 ± 0.12	0.13 ± 0.08	-0.18 ± 0.13
JB204.3	-0.06 ± 0.22	0.12 ± 0.16	0.07 ± 0.10	0.04 ± 0.10	-0.08 ± 0.14
JB204.4	0.11 ± 0.20	-0.10 ± 0.14	0.07 ± 0.10	0.04 ± 0.08	-0.09 ± 0.13
JA-2					
JA2.1	0.27 ± 0.21	0.07 ± 0.16	0.11 ± 0.11	0.07 ± 0.08	-0.04 ± 0.12
JA2.2	-0.10 ± 0.19	-0.03 ± 0.13	0.00 ± 0.09	-0.01 ± 0.09	0.05 ± 0.14
JA2.3	0.33 ± 0.23	0.14 ± 0.16	0.15 ± 0.12	0.02 ± 0.09	-0.06 ± 0.14
JA2.4	0.24 ± 0.21	0.22 ± 0.15	0.16 ± 0.11	0.13 ± 0.08	0.01 ± 0.13
JA2.5	0.19 ± 0.21	0.01 ± 0.16	0.10 ± 0.10	0.08 ± 0.09	-0.01 ± 0.13
JA2.6	0.00 ± 0.20	0.15 ± 0.14	0.07 ± 0.11	0.00 ± 0.08	0.11 ± 0.13
JA2.7	0.14 ± 0.21	0.00 ± 0.14	0.09 ± 0.12	0.13 ± 0.10	-0.20 ± 0.12
JA2.8	0.31 ± 0.19	0.16 ± 0.14	0.14 ± 0.11	-0.02 ± 0.08	-0.21 ± 0.13
JA2.9	0.01 ± 0.23	0.03 ± 0.15	0.11 ± 0.12	-0.02 ± 0.08	0.06 ± 0.14
JA2.10	0.25 ± 0.20	0.07 ± 0.13	0.16 ± 0.10	-0.07 ± 0.09	-0.05 ± 0.11
JA2.11	0.20 ± 0.21	0.06 ± 0.13	0.11 ± 0.10	0.05 ± 0.08	0.16 ± 0.13
DI36.1	0.40 ± 0.19	0.13 ± 0.12	0.30 ± 0.10	0.10 ± 0.08	-0.22 ± 0.14
DI36.2	0.15 ± 0.22	0.05 ± 0.13	0.24 ± 0.10	0.10 ± 0.08	-0.12 ± 0.15
DI36.3	0.11 ± 0.20	0.14 ± 0.11	0.16 ± 0.08	0.13 ± 0.08	-0.23 ± 0.13
DI36.4	0.33 ± 0.21	0.18 ± 0.14	0.04 ± 0.12	0.04 ± 0.09	-0.07 ± 0.14
DI36.5	0.01 ± 0.22	0.02 ± 0.16	-0.02 ± 0.11	0.08 ± 0.09	0.23 ± 0.14
DI36.6	0.05 ± 0.22	0.08 ± 0.17	0.06 ± 0.12	-0.09 ± 0.10	0.14 ± 0.15
JG-1					
DI35.1	-0.13 ± 0.23	0.06 ± 0.17	0.02 ± 0.10	0.11 ± 0.08	-0.04 ± 0.12
DI35.2	-0.11 ± 0.21	-0.05 ± 0.14	0.06 ± 0.09	0.11 ± 0.08	-0.13 ± 0.12
DI35.3	-0.07 ± 0.18	-0.06 ± 0.12	0.14 ± 0.10	0.03 ± 0.08	-0.03 ± 0.14
DI35.4	0.02 ± 0.21	0.06 ± 0.16	0.06 ± 0.12	0.15 ± 0.08	-0.17 ± 0.13
DI35.5	-0.25 ± 0.19	0.00 ± 0.13	-0.02 ± 0.10	-0.02 ± 0.09	-0.08 ± 0.12
DI35.6	0.07 ± 0.17	0.00 ± 0.13	0.09 ± 0.10	0.03 ± 0.07	-0.03 ± 0.11
DI35.7	-0.27 ± 0.18	-0.22 ± 0.12	-0.08 ± 0.10	0.06 ± 0.07	0.15 ± 0.13
W-2a					
W2a.1	0.32 ± 0.21	0.26 ± 0.14	0.09 ± 0.10	0.04 ± 0.09	0.00 ± 0.13
W2a.2	0.00 ± 0.20	0.00 ± 0.13	0.07 ± 0.09	0.05 ± 0.07	-0.13 ± 0.13
W2a.3	0.30 ± 0.20	0.14 ± 0.15	0.12 ± 0.10	0.07 ± 0.08	-0.22 ± 0.12
W2a.4	0.22 ± 0.22	0.13 ± 0.17	0.09 ± 0.10	0.13 ± 0.08	-0.15 ± 0.12
W2a.5	0.00 ± 0.21	0.04 ± 0.15	0.12 ± 0.11	0.04 ± 0.09	-0.09 ± 0.14
W2a.6	-0.07 ± 0.22	-0.03 ± 0.16	0.05 ± 0.10	0.04 ± 0.08	-0.17 ± 0.14
W2a.7	0.14 ± 0.20	-0.02 ± 0.15	0.14 ± 0.10	0.00 ± 0.10	-0.02 ± 0.13
W2a.8	0.02 ± 0.19	0.06 ± 0.14	0.17 ± 0.11	0.10 ± 0.10	-0.01 ± 0.12
W2a.9	-0.24 ± 0.20	-0.15 ± 0.14	0.00 ± 0.10	0.00 ± 0.08	0.00 ± 0.12
W2a.10	0.12 ± 0.22	0.05 ± 0.14	0.06 ± 0.10	0.04 ± 0.08	-0.03 ± 0.15

Mo isotope ratios are normalized to ^{98}Mo/^{96}Mo = 1.453173 and reported relative to the Alfa Aesar bracketing standard. Each line represents a single measurement, which consumed ~80 ng of Mo (run at ~100 ppb). Given uncertainties are two standard errors (2 s.e.) obtained from internal run statistics. BHVO-2: Different numbers (22–26) denote separate digestions of ~0.5 g standard material that were processed through the full chemical separation procedure and analysed with each set of samples. Mean values (±95% CI) for the different rock standards are provided in Supplementary Table 1.

Supplementary Table 3. Leaching procedure applied to the unequilibrated ordinary chondrites NWA 2458 (L3.2) and WSG 95300 (H3.3).

Step	Acid volumes	Acid mixture	Temperature (°C)	Duration (days)
L1	25ml HAc + 25ml H2O	50ml 8.9M HAc	20	1
L2	12.5ml HNO3 + 25ml H2O	37.5ml 5.1M HNO3	20	5
L3	15ml HCl + 17.5ml H2O	32.5ml 5.0M HCl	75	1
L4	15ml HF + 7.5ml HCl + 7.5ml H2O	30ml 14.6M HF – 2.7M HCl	75	1
L5	7.5ml HF + 7.5ml HCl	15ml 14.6M HF – 5.5M HCl	150	3
L6a	14ml HF + 7ml HNO3 + 0.4ml HClO4	21.4ml 19.0M HF – 5.0M HNO3 – 2% HClO4	180-200	5
L6b	14ml HNO3 + 7ml HCl	21ml 10.3M HNO3 – 3.7M HCl	130-170	3

The procedure was modified from ref. 35. See Methods for details.

Supplementary Table 4. Summary of Mo isotope data for bulk meteorites.

Sample	ε^{92}Mo	ε^{94}Mo	ε^{95}Mo	ε^{97}Mo	ε^{100}Mo	Reference
Carbonaceous meteorites						
CI	1.12 ± 0.59	0.79 ± 0.41	0.69 ± 0.23	0.26 ± 0.19	0.44 ± 0.34	37
CM	6.44 ± 0.39	4.82 ± 0.20	3.17 ± 0.16	1.66 ± 0.14	2.28 ± 0.22	37
CO	2.41 ± 0.15	1.66 ± 0.34	1.39 ± 0.34	0.71 ± 0.28	0.97 ± 0.11	47
CV	1.41 ± 0.27	0.97 ± 0.19	0.81 ± 0.05	0.40 ± 0.08	0.44 ± 0.12	12
CK	2.26 ± 0.35	1.63 ± 0.22	1.24 ± 0.15	0.58 ± 0.15	0.73 ± 0.22	this study
CR	4.14 ± 0.12	3.11 ± 0.15	2.26 ± 0.04	1.18 ± 0.04	1.40 ± 0.17	36
CH	2.32 ± 0.11	1.79 ± 0.10	1.29 ± 0.04	0.62 ± 0.09	0.66 ± 0.11	this study
CB	1.53 ± 0.08	1.26 ± 0.04	0.99 ± 0.04	0.51 ± 0.04	0.45 ± 0.04	this study
Eagle Station pallasites	1.14 ± 0.24	0.85 ± 0.32	0.80 ± 0.14	0.41 ± 0.09	0.79 ± 0.15	37
Milton (ungr.)	–	1.30 ± 0.26	1.04 ± 0.09	0.54 ± 0.05	–	48
Tafassasset (ungr.)	2.17 ± 0.15	1.65 ± 0.07	1.20 ± 0.05	0.62 ± 0.05	0.63 ± 0.06	this study
IIC	3.11 ± 0.12	2.22 ± 0.09	1.54 ± 0.06	0.85 ± 0.07	0.96 ± 0.07	13
IID	1.63 ± 0.10	1.16 ± 0.16	0.96 ± 0.15	0.51 ± 0.12	0.67 ± 0.17	13
IIF	1.50 ± 0.21	1.11 ± 0.13	0.94 ± 0.08	0.50 ± 0.08	0.63 ± 0.13	13
IIIF	1.59 ± 0.14	1.20 ± 0.11	0.99 ± 0.04	0.55 ± 0.06	0.61 ± 0.09	13
IVB	2.47 ± 0.76	1.55 ± 0.22	1.17 ± 0.10	0.57 ± 0.03	0.84 ± 0.33	15
South Byron Trio (SBT)	–	1.27 ± 0.07	1.03 ± 0.04	0.49 ± 0.02	–	48
Grand Rapids (ungr.)	1.28 ± 0.62	1.15 ± 0.40	0.89 ± 0.25	0.45 ± 0.25	0.48 ± 0.36	49
Mbosi (ungr.)	1.17 ± 0.67	1.10 ± 0.43	1.02 ± 0.27	0.50 ± 0.20	0.63 ± 0.25	37
Wiley (ungr.)	4.47 ± 0.22	3.49 ± 0.13	2.34 ± 0.11	1.21 ± 0.11	1.41 ± 0.14	13
Non-carbonaceous meteorites						
OC	0.66 ± 0.08	0.61 ± 0.06	0.25 ± 0.06	0.11 ± 0.05	0.14 ± 0.08	50
EC	0.38 ± 0.06	0.36 ± 0.05	0.14 ± 0.03	0.09 ± 0.02	0.14 ± 0.03	50
RC	0.45 ± 0.15	0.42 ± 0.10	0.18 ± 0.05	0.08 ± 0.05	0.11 ± 0.12	this study
Acapulcoites	1.01 ± 0.24	0.94 ± 0.12	0.41 ± 0.07	0.26 ± 0.08	0.26 ± 0.11	this study
Lodranites	1.48 ± 0.90	1.10 ± 0.30	0.48 ± 0.15	0.21 ± 0.03	0.24 ± 0.22	15
Winonaites	0.30 ± 0.28	0.22 ± 0.10	0.07 ± 0.04	0.02 ± 0.09	0.03 ± 0.06	15
Brachinites	1.33 ± 0.15	1.12 ± 0.15	0.58 ± 0.08	0.33 ± 0.04	0.32 ± 0.09	this study
Ureilites	0.98 ± 0.12	0.89 ± 0.09	0.38 ± 0.04	0.21 ± 0.03	0.15 ± 0.07	this study
EET 87517 (anom. ureilite)	1.90 ± 0.35	1.62 ± 0.22	0.83 ± 0.15	0.48 ± 0.15	0.47 ± 0.22	this study
PCA 82506 (anom. ureilite)	2.04 ± 0.35	1.35 ± 0.22	0.73 ± 0.15	0.30 ± 0.15	0.40 ± 0.22	this study
Angrites	0.78 ± 0.28	0.75 ± 0.11	0.39 ± 0.06	0.26 ± 0.10	0.07 ± 0.12	this study
Aubrites	0.56 ± 0.13	0.48 ± 0.05	0.25 ± 0.06	0.19 ± 0.03	0.16 ± 0.10	this study
Mesosiderites	1.21 ± 0.14	1.04 ± 0.08	0.46 ± 0.05	0.25 ± 0.03	0.19 ± 0.04	this study
Main group pallasites	1.06 ± 0.34	0.85 ± 0.22	0.38 ± 0.14	0.16 ± 0.09	0.20 ± 0.20	37
NWA 725 (ungr.)	1.55 ± 0.68	1.20 ± 0.24	0.52 ± 0.16	0.30 ± 0.05	0.63 ± 0.30	15
NWA 1058 (ungr.)	1.61 ± 0.12	1.31 ± 0.11	0.68 ± 0.09	0.38 ± 0.10	0.40 ± 0.08	this study
IAB (MG, sL)	-0.03 ± 0.30	0.04 ± 0.10	-0.07 ± 0.05	0.00 ± 0.02	0.02 ± 0.03	11
IAB (sH)	0.96 ± 0.65	0.94 ± 0.27	0.38 ± 0.13	0.24 ± 0.02	0.24 ± 0.17	15
IC*	0.97 ± 0.68	0.88 ± 0.26	0.36 ± 0.06	0.22 ± 0.05	0.29 ± 0.11	11, 13
IIAB	1.52 ± 0.86	1.20 ± 0.22	0.55 ± 0.16	0.26 ± 0.07	0.35 ± 0.18	11
IIE	0.86 ± 0.32	0.71 ± 0.15	0.29 ± 0.13	0.12 ± 0.07	0.24 ± 0.07	14
IIIAB	1.35 ± 0.69	1.07 ± 0.24	0.44 ± 0.15	0.24 ± 0.04	0.44 ± 0.24	11
IIIE*	1.33 ± 0.15	1.01 ± 0.14	0.50 ± 0.10	0.28 ± 0.08	0.30 ± 0.11	13, 14, 37
IVA	0.99 ± 0.79	0.80 ± 0.28	0.37 ± 0.13	0.19 ± 0.06	0.24 ± 0.30	11
Gebel Kamil (ungr.)	0.31 ± 0.91	0.34 ± 0.30	0.07 ± 0.15	0.04 ± 0.08	0.32 ± 0.22	11

Mo isotope data (normalized to ^{98}Mo/^{96}Mo) and references for bulk meteorites as displayed in Fig. 1 and used for calculations of the CC- and NC-lines. *Combined mean of samples with small or no CRE effects.

References in Supplementary Information

38. Goderis, S., Brandon, A. D., Mayer, B. & Humayun, M. s-Process Os isotope enrichment in ureilites by planetary processing. *Earth Planet. Sci. Lett.* **431**, 110-118 (2015).
39. Yokoyama, T., Alexander, C. M. O. D. & Walker, R. J. Assessment of nebular versus parent body processes on presolar components present in chondrites: Evidence from osmium isotopes. *Earth Planet. Sci. Lett.* **305**, 115-123 (2011).
40. Burkhardt, C., Kleine, T., Dauphas, N. & Wieler, R. Origin of isotopic heterogeneity in the solar nebula by thermal processing and mixing of nebular dust. *Earth Planet. Sci. Lett.* **357-358**, 298-307 (2012).
41. Dauphas, N., Marty, B. & Reisberg, L. Molybdenum Nucleosynthetic Dichotomy Revealed in Primitive Meteorites. *Astrophys. J.* **569**, L139-L142 (2002).
42. Weis, D. *et al*. High-precision isotopic characterization of USGS reference materials by TIMS and MC-ICP-MS. *Geochem. Geophys. Geosyst.* **7**, Q08006 (2006).
43. Hin, R. C., Burkhardt, C., Schmidt, M. W., Bourdon, B. & Kleine, T. Experimental evidence for Mo isotope fractionation between metal and silicate liquids. *Earth Planet. Sci. Lett.* **379**, 38-48 (2013).
44. Greber, N. D., Puchtel, I. S., Nägler, T. F. & Mezger, K. Komatiites constrain molybdenum isotope composition of the Earth's mantle. *Earth Planet. Sci. Lett.* **421**, 129-138 (2015).
45. Marchi, S., Canup, R. M. & Walker, R. J. Heterogeneous delivery of silicate and metal to the Earth by large planetesimals. *Nature Geosci.* **11**, 77-81 (2018).
46. Wade, J., Wood, B. J. & Tuff, J. Metal-silicate partitioning of Mo and W at high pressures and temperatures: Evidence for late accretion of sulphur to the Earth. *Geochim. Cosmochim. Acta* **85**, 58-74 (2012).
47. Burkhardt, C., Hin, R. C., Kleine, T. & Bourdon, B. Evidence for Mo isotope fractionation in the solar nebula and during planetary differentiation. *Earth Planet. Sci. Lett.* **391**, 201-211 (2014).
48. Hilton, C. D., Bermingham, K. R., Walker, R. J. & McCoy, T. J. Genetics, crystallization sequence, and age of the South Byron Trio iron meteorites: New insights to carbonaceous chondrite (CC) type parent bodies. *Geochim. Cosmochim. Acta* **251**, 217-228 (2019).
49. Dauphas, N., Marty, B. & Reisberg, L. Molybdenum Evidence for Inherited Planetary Scale Isotope Heterogeneity of the Protosolar Nebula. *Astrophys. J.* **565**, 640-644 (2002).
50. Render, J., Fischer-Gödde, M., Burkhardt, C. & Kleine, T. The cosmic molybdenum-neodymium isotope correlation and the building material of the Earth. *Geochem. Persp. Let.* **3**, 170-178 (2017).

Supplementary Data 1

Data file for Supplementary Table 4. Summary of Mo isotope data and references for bulk meteorites as displayed in Fig. 1 and used for calculations of CC- and NC-lines.